Article:

Childs, THC, Arrazola, P-J, Azpitarte, L et al. (4 more authors) (2022) Physical modelling with experimental validation of high ductility metal cutting chip formation illustrated by copper machining. International Journal of Machine Tools and Manufacture, 173. 103847. ISSN 0890-6955

https://doi.org/10.1016/j.ijmachtools.2021.103847

eprints@whiterose.ac.uk
https://eprints.whiterose.ac.uk/

Physical modelling with experimental validation of high ductility metal cutting chip formation illustrated by copper machining

Thomas H.C. Childs[a*], Pedro-J Arrazola[b], Larraitz Azpitarte[b], Ainhara Garay[b], Denis Soriano[b], Mikel S-de-Buruaga[b], Mikel Cuesta[b],

[a]: School of Mechanical Engineering, University of Leeds, Leeds LS29JT, UK
[b]: Faculty of Engineering, Mondragon University, Mondragon 20500, Spain
*: corresponding author: t.h.c.childs@leeds.ac.uk

Abstract.

This paper addresses problems of predicting chip formation in high strain machining conditions. A complete physical model of chip formation requires both plasticity and chip/tool friction models. Friction models are commonly partly phenomenological, with friction coefficients measured from the conditions in which the models are applied. This paper's thesis is that friction emerges from the plastic response of the chip material in contact with the cutting tool. Extremely large strains are generated in the contact region. In the case of machining highly ductile metals large strains also occur in the bulk of the chip. This paper applies a Mechanical Threshold Stress plasticity model extended to high strains (equivalent strains > 5) to simulating chip formation in copper machining, without assuming measured values of friction coefficients. In the case of copper machining there is not a unified source of experimental knowledge against which to validate simulations. There is a need to provide such a source. This paper reports extensive results from machining three coppers in general engineering conditions. At all cutting speeds there remains a systematic difference between the simulated and experimental chip thicknesses. In addition, at low cutting speeds an experimental observation is that chip formation cycles between low and high thicknesses. The simulations do not predict this. The experiments show the cycling to occur when the chip thickness rises to 10 or more times the uncut thickness. It is speculated with some evidence that the cycling is associated with plastic failure rather than with strain hardening, as is currently commonly given as the explanation. Modelling large strain plasticity and failure of highly ductile metals, for metal machining simulations, remains incomplete.

Author email addresses: t.h.c.childs@leeds.ac.uk (corresponding author), pjarrazola@mondragon.edu, lazpitarte@mondragon.edu, agaray@mondragon.edu, dsoriano@mondragon.edu, msaez@mondragon.edu, mcuesta@mondragon.edu

Keywords Metal machining; Mechanical Threshold Stress model; Friction model; Force measurement; Chip thickness measurement; Hardness testing

Nomenclature

ECAP	Equal channel angular pressing
HPT	High Pressure Torsion
MTS	Mechanical Threshold Stress (model)
B	Burgers vector (Eqs. 5a and 6b)
g_0	Normalized activation energy (Eq. 5a)
h	Uncut chip thickness
k	Shear plane shear stress
k_b	Boltzmann constant (Eqs. 5a and 6b)
k_0	Stress constant (Eq.6b)
p, q	Coefficients (Eq. 5a)
r_β	Cutting edge radius
t	Chip thickness
s	Activation factor (Eqs. 3a, 5a and 5b)
v_c	Cutting speed
w	Uncut chip width
A	Dimensionless coefficient (Eq. 6b)
A5	% elongation to failure, test length 5x diameter
C_3, C_4	Coefficients (Eq. 5b)
F_C, F_T	Cutting and thrust force
$F_C{}^*, F_T{}^*$	Specific cutting and thrust force
HV	Vickers hardness
T	Temperature
$T_{a,zero}$	Temperature at which α_{IV} becomes zero (Eq. 9b)
R_m	Tensile strength
$R_{p0.2}$	0.2% offset yield stress
α	Tool clearance angle
$\alpha_{IV}, \alpha_{IV,20}$	A parameter of Eq. 9a, and its value at 20°C
β	A coefficient of Eq. 9a
γ	Tool rake angle
$\bar{\varepsilon}$	Equivalent strain
$\bar{\varepsilon}_{lower}, \bar{\varepsilon}_{upper}$	Maximum and minimum strain values in Eq. 10
$\dot{\bar{\varepsilon}}$	Equivalent strain rate
$\dot{\bar{\varepsilon}}_0$	Reference strain rate (Eq. 5a)
$\dot{\bar{\varepsilon}}_{\eta,0}$	Reference strain rate (Eq. 6b)
η	Saturation stress of the MTS model
$\theta_1, \theta_2, \theta_3,$	Coefficients of the function θ (Eq. 6b)
λ	Friction angle
μ_f	Friction coefficient
μ_T, μ_0	Elastic shear modulus at temperatures T and 0K
σ_a	Constant stress term of the MTS model (Eq. 3a)
σ_n	Normal contact stress between chip and tool
σ_t	Threshold stress (MTS model)
$\sigma_{t,\ initial}$	Initial value of the threshold stress
$\bar{\sigma}$	Equivalent stress (plastic flow stress)
τ_{fric}	Friction stress between chip and tool
$\chi, \chi_{min}, \chi_{max}$	Parameter of Eq. 10 with its minimum and maximum values
ϕ	Shear plane angle

1. **Introduction**

The origins of this paper lie in a conversation at a symposium on physical modelling of copper plasticity. It was asked what are the fundamental problems in applying physical modelling to predictions of chip formation during machining highly ductile metals such as annealed copper? This paper addresses this question, at least in part, through developing physical based simulations and comparing the results with experiments.

An initial issue is the scarcity and scattered nature of published experimental data on copper chip formation. Copper machining has not received much academic attention for its own sake (an exception is the ultra-precision turning of copper with single crystal diamond tools to produce mirror-finish surfaces; this low feed application is outside the scope of the present paper). The reason is that there are few practical problems in copper machining. Annealed copper is well-known to be an unsatisfactory metal to machine at general engineering feeds and low cutting speeds ($v_c <$ 50m/min), with low rake angle tools ($\gamma < 10°$). Very large strains occur in the chip (the ratio of chip thickness t to uncut thickness h can reach 10 or more), leading to high cutting forces and large burr formation. In practice these problems are avoided by using higher cutting speeds and larger rake angle tools. Instead, research into copper machining has often been carried out to serve other purposes.

Mainly from the 1950s to the 1970s, during the early development of chip formation models, with the focus on predicting cutting and thrust forces, copper was just one of many metals chosen for studying the relationship between the chip thickness ratio, the tool rake angle and the sliding friction coefficient between chip and tool.

Mainly within the last 10-15 years the stability of copper microstructure in high strain processes such as equal channel angular pressing (ECAP) and high pressure torsion (HPT) has become of interest to researchers. Machining has been recognised as another high strain process. The hardness and microstructure of copper chips have been studied experimentally, mainly but not exclusively, for their relevance to ECAP and HPT.

Only rarely do the recent microstructural studies also report all three of cutting and thrust forces and chip thickness ratio. It was decided that the experimental studies mainly from the 1950s-1970s needed to be updated taking into account subsequent knowledge from microstructural studies. The experimental studies reported in this paper are of value for their own sake.

Over the past 10 years, and of particular relevance to this paper, physically based constitutive models of plastic flow have started to replace phenomenological models as inputs to numerical simulations of chip formation. How to extend physical models to the high strain, strain rate and temperature conditions of chip formation, particularly to the conditions at the chip/tool interface, is

an ongoing area of study. Copper is chosen as a material for such studies because the dependence of its strain hardening on the underlying evolution of its dislocation structures is relatively well-understood, established from the early 1990s onwards. Modelling and simulation has also developed to include plastic inhomogeneity at a grain size level.

Physical modelling of chip formation needs friction modelling as well as plasticity modelling. A limitation of much previous work is that it requires the friction interaction between chip and tool to be input as known parameters of a phenomenological friction law. This paper's thesis is that the friction condition should emerge as part of the solution, from the copper plasticity's dependence on strain, strain rate and temperature at the chip/tool interface. The modelling and simulation studies reported in this paper cover both plasticity and friction modelling.

The previous works on which this paper is based are reviewed in the following three sub-sections of this Introduction.

1.1. *Cutting and thrust force and chip thickness ratio measurements.*

The conditions of experimental studies of chip formation when machining annealed copper in the absence of cutting fluids, from which it has been possible to extract all three of cutting and thrust force and chip thickness ratio, are listed in Table 1. All are for the turning of round bar or for axial feeding to reduce the length of a rotating tube, except for E which is linear cutting of plate. The sources A-E are pre-1980 [1-7]. Only F is recent [8,9]. The copper specification (as far as is known) and what is the tool material (high speed steel in all cases) are given. In addition to v_c, h and γ, already defined, the uncut chip width w is given. For chip formation to be near to plane strain (the condition to be simulated here), w should be substantially larger than t, the chip thickness.

The cases A, B, E certainly meet the plane strain condition but A contains only summary data from a now unavailable 1952 report. The grade of copper is not specified beyond 'high conductivity'. B provides excellently detailed information but its work material is 97.8% Cu (probably the remainder is Zn but it is not mentioned). The conditions of C and D are far from orthogonal. Chip thicknesses almost as large as the uncut chip width are reported, with a large consequent side flow. The main interest of F is not forces and chip thickness but microstructural evolution (see Section 1.2). Its w/h value is close to those of C and D. Information is not given on the state of its anneal. (E contains additional data from machining hard rolled 99.999% Cu, which is introduced in Section 1.2)

Force and chip thickness ratio results from all these works are presented in Fig. 1. Forces are plotted as specific cutting and thrust forces $F_C{}^*$, $F_T{}^*$, i.e forces per unit uncut chip cross-section area. The chip thickness results from C and D are increased from their measured values as if there were no

4

side flow but maintaining the chip cross-section areas unchanged (in C thickness was measured by micrometer and in D from sectioned chips).

All of F_C*, F_T* and t/h reduce with increasing cutting speed. It is expected, other things being equal, that they also reduce with increasing γ. This is not seen. Although C and D ($\gamma = 6°$) have the highest values, E and F ($\gamma = 0$ and 5°) have the lowest. There is little difference between A and B ($\gamma = 10$ and 20°).

Table 1. The conditions of annealed copper dry machining tests, with their sources. The sources are papers with data on cutting and thrust forces and chip thickness ratios.

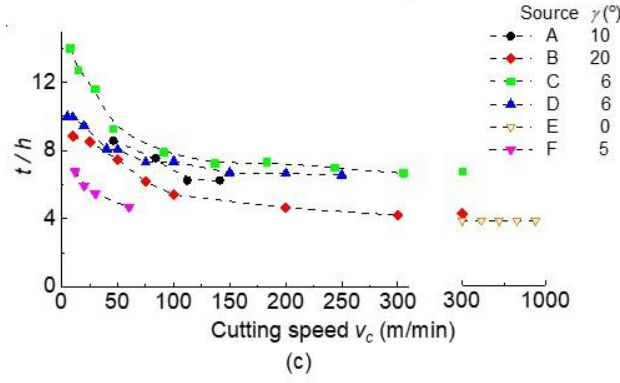| Materials		Process					
Work	Tool	v_c (m/min)	h (mm)	w (mm)	γ (°)	Source	
high conductivity Cu	HSS	45-140	0.16	6.35	10	A [1,2]	
97.8%Cu, 55HB	HSS	10-500	0.13	4.6	20	B [3]	
ETP(99.85%)Cu, 85HV	HSS	7.5-300	0.16	1.3	6	C [4]	
commercially pure, 83HV	HSS	5-250	0.2	1.25	6	D [5]	
ETP (99.93%)Cu, 56HV	HSS	300-900	0.25	6.1	0	E [6,7]	
OFHC Cu	HSS	12-60	0.3	2.0	5	F [8,9]	

(a)

(b)
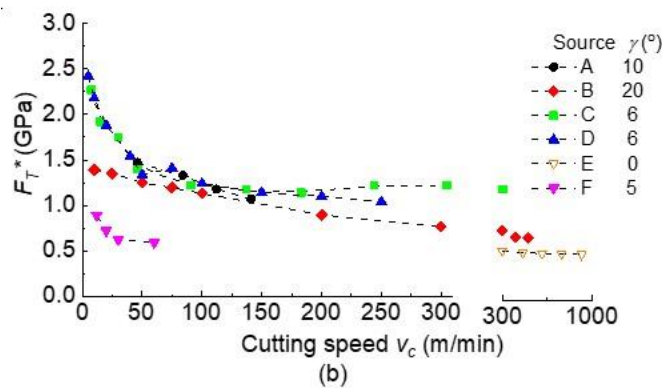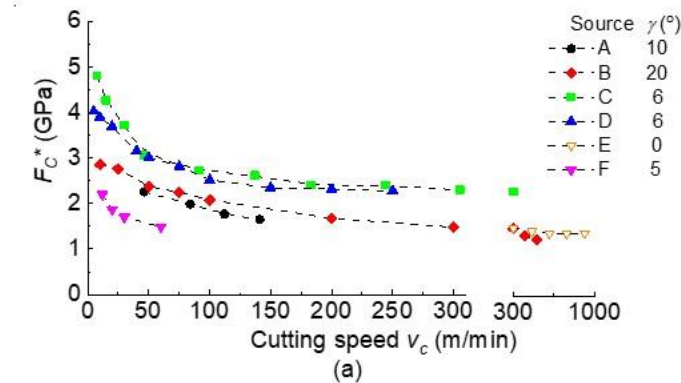
Fig. 1. Dependence on cutting speed of chip formation variables. (a) Specific cutting force. (b) Specific thrust force. (c) Chip thickness ratio. The sources A-F are from Table 1. The colour code is to guide the eye and is carried forward to Figs. 2 and 3.

The results A-F are further usefully analysed in terms of the shear plane description of chip formation even though this description is well-known to be an oversimplification. In reality chip formation occurs by shear in a zone of finite width and the predictive values of the minimum energy (Merchant [10]) and slip line (Lee and Shaffer [11]) shear plane models are low. The descriptive value remains useful because it supports considerations of whether changes with cutting conditions of easily measured forces and chip thickness ratios are caused by changes in the work material's plasticity or by changes in its friction interaction with the cutting tool. When results from modelling and simulation are compared with experimental results, it similarly supports whether differences are due to mistaken plasticity or mistaken friction modelling.

As is well-known [10,11], the shear plane description takes chip formation to be by shear on a plane inclined at the angle ϕ to the cutting direction. The forces F_C and F_T resolved on to the shear plane generate the plastic shear flow stress k. ϕ depends geometrically on t/h and γ. The resultant of the forces is inclined at the friction angle λ to the normal to the rake face. Eq.1 summarises the derived relationships (with F_C and F_T the forces per unit length along the cutting edge).

$$tan\,\phi = \frac{cos\,\gamma}{t/h - sin\,\gamma}; \qquad k = \frac{\left(F_C\,cos\,\phi - F_T\,sin\,\phi\right)sin\,\phi}{h}; \qquad \lambda = tan^{-1}\left(\frac{F_T}{F_C}\right) + \gamma \qquad (1)$$

From slip line modelling it is expected that $(\phi - \gamma)$ is some function of λ under changing cutting conditions. Fig. 2a re-plots the data of Fig. 1 as the dependence of $(\phi - \gamma)$ on λ (this differs from the more usual plot of ϕ versus $(\lambda - \gamma)$ that is suggested by Merchant's minimum energy model). $(\phi - \gamma)$ is seen generally to reduce with increasing λ, as expected. There is also a wide range of λ: 43-48° for A and B, 30-37° for C and D, reducing to 25-27° for F and 20° for E. This large range of λ is returned to in Section 1.3.

6

From the strain hardening behaviour of metals k varies only slowly with cutting speed, mainly dependant on shear plane temperature. Fig. 2b re-plots the data of Fig. 1 as the dependence of k on v_c. $k = 310\pm30$MPa in all cases except for A, for which $k \approx 250$MPa. The cause of this lower value of k is not known. At least it explains why the forces (Fig. 1) for cases A and B are approximately the same when the lower rake angle in the case of A than B leads to the expectation that its forces should be higher than B's: A's lower k lowers that expectation. And considering only the cases B-F, differences in their forces and chip thickness ratios (Fig. 1) come entirely from differences in their λ (Fig. 2a) and γ values.

In the present work the experimental and simulated dependences of F_C^*, F_T^* and t/h on v_c will be considered directly. They will also be transformed to dependences of $(\phi - \gamma)$ on λ and of k on v_c in order to assess whether changes with v_c and differences between them are due to changes and differences in the work and chip plastic flow stress or in the chip/tool friction interaction.
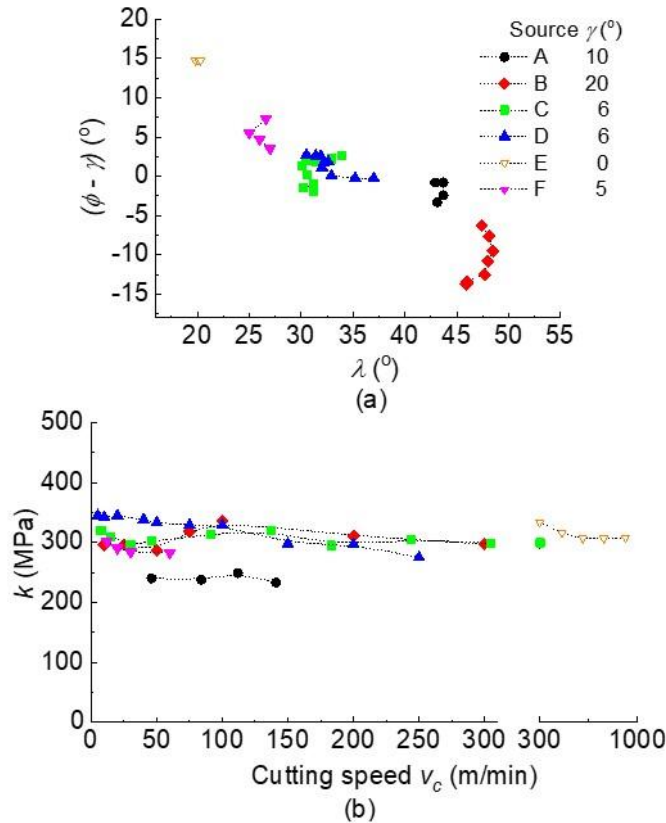

Fig. 2. Transformations of the data in Fig. 1. (a) The dependence of $(\phi - \gamma)$ on λ. (b) The dependence of k on cutting speed. The symbols in (b) are the same as in (a).

Finally, in this Section it is appropriate to introduce a small number of further experimental studies of chip formation even though they do not all meet the criterion of presenting data on all three of cutting and thrust force and chip thickness ratio.

All the works [1-9] describe the chip formation at all cutting speeds as continuous. A recent paper [12] describes the chip formation resulting from feeding a tool radially into a rotating disc. Thick chips ($t/h \approx 15$) and thin chips ($t/h \approx 3$) are formed alternately from one rotation of the disc to the next. The work material is annealed (68HV) 99.99% OFHC copper. $\gamma = 0°$, h is in the range 0.05 to 0.1mm and v_c in the range 0.6 to 3.6m/min. Cyclical chip formation has been reported before, in a paper from 1974 [13]. In that case the work material was annealed 70/30 brass but it is written that the same cyclical chip formation occurs with copper, as well as with annealed aluminium, austenitic stainless steel and titanium. The cyclical chip formation was observed over the applied range of $v_c =$ 4.7m/min, $h = 0.02$-0.11mm and γ from -10 to +10°. In both [12] and [13] the explanation for the cyclical formation is given that during thick chip formation with annealed work the straining beneath the cut surface is so large that the next pass of the tool is as over a strain hardened material; then the sub-surface straining is sufficiently low that the following pass is through less strained material; and so on without end. The question arises: why did cyclical chip formation not occur in the works [1-9]?

Values of F_C* and F_T* are not given in [12]. Values can be extracted from other work from the same group, though for a different cutting condition [14]. In a single pass over an annealed material (68HV, 99.99% copper), with $\gamma = 0°$, $v_c = 0.03$m/min, $h = 0.05$mm and $w = 3$mm, t/h is given as $\approx$ 10. $F_C \approx 800$N and $F_T \approx 0.25F_C$. $F_C* \approx 5.3$GPa and $F_T* \approx 1.3$GPa are obtained from these. λ, $(\phi - \gamma)$ and k are calculated to be $\approx 14°$, $6°$ and 510MPa. Particularly k is significantly larger than values in Fig. 2b. The λ, $(\phi - \gamma)$ pairing is an extension to lower values of λ of the results in Fig. 2a.

These studies also identify a mechanism other than strain hardening that causes cyclical chip formation. A transition from a thick to a thin chip is caused by applying a surface active coating to material to be cut, for both 70/30 brass [13] and copper work materials [15, 16]. In an example of machining a 99.99% OFHC copper at $v_c = 0.12$m/min, with $\gamma = 0°$, $h = 0.05$mm and $w = 2.3$mm, a surface coating reduces F_C*, F_T* and t/h from 3.8GPa, 3.1GPa and 12 to 1.45GPa, 1.7GPa and 8. The thin chip becomes embrittled and segmented. $k = 294$MPa and $\lambda = 39°$ are calculated here for the thick chip and $k = 150$MPa, $\lambda = 49°$ for the thin chip.

It is argued in [14] and [16] and in a series of other papers, for example [17, 18], that the conditions of flow during thick chip formation are so far from those approximated in the shear plane model that analysis in terms of that model is inappropriate. Particle image velocimetry (PIV) reveals the chip formation to be by a non-steady, sinuous, flow and folding in a manner that is better described by surface buckling of the work material ahead of the tool. It is another reason for revisiting experimentally the cutting conditions of Table 1, generally at higher speeds than those of [12-17].

1.2. *Hardness and microstructure observations.*

It is now recognized from micro- and nano-hardness studies, and also from transmission and scanning electron microscopy, that the microstructures of chips formed from machining annealed copper vary with the chip thickness ratio (strain) and cutting speed (strain rate and temperature). These determine the straining, recovery and recrystallization structural changes that occur in the chips and which also give rise to chip hardness changes.

In experiments with annealed (73HV) 99.999% copper, with v_c from 0.8 to 270m/min, $h =$ 0.21mm and γ ranging probably at least over 0-30° (exact values are not given), the Vickers microhardness (200g load) of chips is measured from $\approx$ 140kg/mm^2 at low cutting speeds to 75kg/mm^2 in the most severe conditions [19]. Fig.3, adapted from [19], divides the shear strain / cutting speed space into 4 regions in which hardness takes different levels, 145-160HV in region *I*, 130-145HV in region *II*, 80-130HV in region *III*, and <80HV in region *IV*. The positions of the region *II/III* and *III/IV* boundaries at low speed and high strain are unclear. For v_c < 10m/min, hardness in the range 120 to 145kg/mm^2 is observed up to the highest strains of $\approx$ 14. The III/IV boundary in Fig. 3 for v_c > 270m/min is an extrapolation. The microstructures in regions *I* and *II* and at v_c < 10m/min are typical of strain hardening to various degrees. Region *IV* shows dynamically recrystallized structures and region *III* shows partial dynamic recrystallization.

In [19] shear strain is estimated from the shear plane model of chip formation. The given equation can be re-written as $[(t/h) \cos\gamma / \cos^2(\phi - \gamma)]$. For the experimental conditions of Fig. 1, shear strain closely equals t/h. The results of Fig. 1c can therefore be transposed directly on to Fig. 3. In all cases, except for F, chip formation lies near to or above the *III/IV* boundary.

The machining conditions of works (in addition to [19]) that consider hardness and / or microstructural change in copper chips are listed in Table 2 (E and F are repeated from Table 1). G's condition is linear cutting of plate (w is not given), H's is axial feeding to reduce tube and I's is fly-cutting (intermittent linear cutting of plate). The chip shear strain / cutting speed combinations from these sources are also added to Fig. 3. G spans the regions *I* to *IV* up to v_c = 75m/min. H is a single result. However, just as A-D do not consider chip hardness and microstructure, G-I (and also [19]) do not report cutting and thrust forces (with one exception: H's single result gives F_C* = 1.6GPa, F_T* = 1.3GPa, t/h = 6.8, from which λ, $(\phi - \gamma)$ and k are calculated to be 34°, 13.5° and 200MPa). The only works that consider in detail both forces and chip condition other than shear strain are E and F. There is a mismatch in the information from A-D and G-I.

Table 2. Further conditions of annealed copper dry machining tests, with their sources. The sources are papers with data on microstructural changes during machining (further data are in [19].

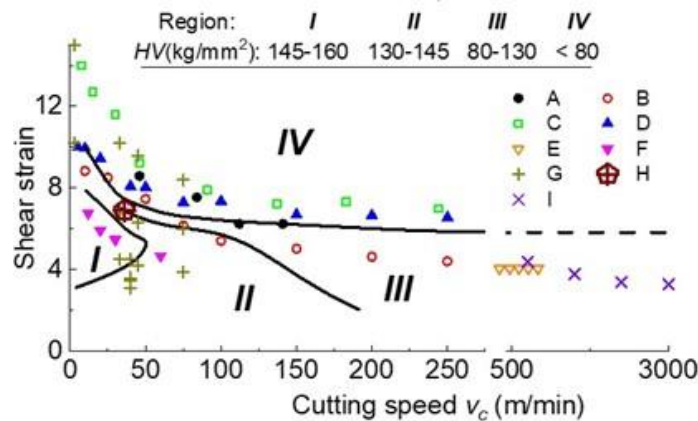| Materials		Process				Source
Work	**Tool**	v_c (m/min)	h (mm)	w (mm)	γ (°)	
ETP (99.93%) Cu, 56HV	**HSS**	300-900	0.25	6.1	0	E [6,7]
OFHC Cu	**HSS**	12-60	0.3	2.0	5	F [8,9]
commercially pure Cu, 46HV	**HSS**	3-75	0.17	-	0-40	G [20-22]
hot extruded ETP Cu, 68HV	**ceramic**	36	0.25	3	- 5	H [23-25]
annealed OFHC Cu	**carbide**	750-3000	0.15	3	0	I [26,27]

Fig. 3. Chip shear strain dependences on cutting speed. The sources A to I are from Tables 1 and 2. The superposed boundaries (thick lines) separate the regions *I* to *IV* in which different chip hardness levels are reported in [19]. The *III*/*IV* boundary (dashed line) for v_c > 250m/min is an extrapolation.

It is possible that the *III*/*IV* boundary position depends on the purity of the copper. If the boundary, established for 99.999%Cu, were unchanged for the commercial purity copper tested in G, chip hardness < 80HV is expected from G at a shear strain > 8. Instead 150-160HV is reported in all conditions except at a shear strain of 8.5 and v_c = 75m/min. Then chip hardness is 109HV. Evidence for the importance of purity is also found from results of HPT tests. With a copper of >99.99% purity, strain softening from 150HV to 80HV is found as shear strain increases from ≈ 4 to 14 [28] but for a copper of 99.97% purity this softening does not occur [29]. The conditions of A-D are within this range of possible sensitivity of chip hardness to purity of the copper.

It is important for the mechanics of chip formation to ask whether strain-dependent softening occurs during the chip formation, in the primary plastic shear region, or later, in the formed chip. This question is implicitly addressed in E and explicitly in F. In E a chip hardness of 90-110HV is recorded for the 99.93%Cu when the shear stress k ≈ 300MPa (Fig. 2b). E also includes data from machining a hard rolled (120-126HV) 99.999% copper. Chip hardness is measured to be 55-60HV when k is calculated to be ≈ 440MPa. There is no proportionality between the value of k acting

10

during chip formation and the chip hardness measured after formation. Discussion in E, about the influence of cooling rates on final hardness clearly implies that the authors believe that softening occurs during cooling, after the chip formation. In F the microstructures of chips cooled naturally in air and of chips quenched by rapid immersion in water show greater transformation in the former than the latter case. Furthermore, modelling reviewed in Section 1.3 gives $k \approx 300$MPa as a level to be expected of highly strained copper, without strain softening, at the strain rates and temperatures in the chip formation primary shear zone. All these indicate that recrystallization structures / softening in the bulk of the chip develop after chip formation.

It is also important for the mechanics of chip formation whether strain-dependent softening occurs in the secondary shear zone at the chip / tool contact during or after the chip formation; and what changes occur in the cut surface from which a chip is formed during the next pass of the tool. The strains and temperatures in the secondary shear zone are all much greater than in the primary shear zone. The time for material to transit the secondary zone is also greater than the time to transit the primary zone. Direct measurements of shear stress (friction stress τ_{fric} between chip and tool) are scarce. A split-tool test with $\gamma = 20°$, $v_c = 50$m/min and $h = 0.2$mm gives a plateau friction stress τ_{fric} = 250±25MPa when $k = 340$MPa [30]. A restricted contact test in E (contact length = 0.75 x chip thickness) gives the average friction stress $\tau_{fric} = 130$MPa when $k = 300$MPa. Whether these low values of τ_{fric} relative to k involve strain-softening or are simply due to temperature cannot be resolved. Recently however F [9] has reported nano-hardness measurements that show a lower hardness in the secondary shear zone than in the bulk of the chip. It is likely that strain softening does occur during secondary shear. In the present work it is found not to be necessary to include strain softening in modelling deformation in the primary shear zone but it is necessary in the secondary zone (see Section 5).

It is difficult to preserve the cut surface for subsequent hardness and micro-structural study in conditions such as turning in which a tool feeds progressively over the surface. Stopping the cut normally leaves the cut surface in a transient condition. As a result, most cut surface studies are from short distance, one pass at a time, linear cutting tests or from slow speed cutting when quick-stopping can be successfully applied. Cut surface hardening of annealed copper is universally reported, but to varying degrees and depths below the surface. In linear cutting tests at $v_c = 2.3$m/min, h from 0.04-0.4mm, γ from 15 to 35°, on a copper of bulk Knoop hardness 50kg/mm^2, hardened layer thickness from 5-20h is reported, with maximum hardness at the surface of 130HK [31]. In tests at a higher speed, $v_c = 90$m/min, h from 0.05-0.2mm, $\gamma = 20$ and 30°, on a copper of bulk Brinell hardness 46kg/mm^2, hardened layer thickness is from 5-10h, with a surface hardness ≈ 110HV [32]. But a hardened layer depth of only 1-2h, with a surface hardness of 140HV, is recorded at low speed ($v_c =$

0.6m/min) in [33], and an even higher hardness (190HV) and hardened depth < *h* in [34]. Hardened layer depth < *h* is also reported in [9] and works that deduce hardened depth from measurements of sub-surface strains also derive depths of 1-2*h* [12, 34, 35]. In [13] hardening to a depth ≈ 6*h* is measured for both the thick and thin cycles of chip formation, though this value is for annealed 70/30 brass. In one case, with v_c from 750-3000m/min, dynamic recrystallization is reported in the cut surface, to a depth of 10μm (*h* = 0.15mm, *γ* = 0°) [27].

This range of observations is another reason for revisiting chip formation experimentally with measurements of all of forces and chip thickness, and at least hardness both in the chip and in the cut surface.

1.3. *Modelling and simulation.*

Annealed OFHC copper is one of the materials originally studied by Johnson and Cook in developing their (J-C) metal plasticity model [36]. It equates flow stress to the current strain, strain rate and temperature state of the metal. It remains the most commonly used model in finite element simulations of annealed copper chip formation, either without alteration and with the originally determined coefficients [25] or with further developments but keeping the original coefficients, for example for the prediction of strain, strain rate and temperature distributions that are input to further simulations of micro-structural change [26, 37]; or to model the deformation within individual grains of a multi-grain material model [16, 38, 39]; or with the addition of a failure law and modification to include strain softening, and determining new coefficients by calibration [40].

An alternative modelling, only recently applied to annealed copper machining, equates the flow stress to the stress needed to overcome obstacles to the movement of dislocations within the metal. The strain in models such as the J-C model is replaced by some representation of the current micro-structure. Such physically-based models combine two sub-models, a structure model and a structure evolution model. One form is the mechanical threshold stress (MTS) model. The structure is represented by the stress (the threshold stress) required for plastic flow of the metal at absolute zero temperature. The structure model is written most generally as Eq. 2a and the evolution model as Eq. 2b, where σ_t is the threshold stress. $\bar{\sigma}$ is the flow stress, $\dot{\bar{\varepsilon}}$ is the strain rate and *T* is the absolute temperature. $\bar{\varepsilon}$ is the strain and occurs only in the evolution model. Flow stress is obtained by integrating σ_t along a strain path, from its initial to its current state (as expressed in Eq. 2c for straining starting from a non-zero initial threshold stress), before substituting it in Eq. 2a.

$$\bar{\sigma} = f_1\left(\sigma_t, \dot{\bar{\varepsilon}}, T\right) \tag{2a}$$

$$d\sigma_t/d\bar{\varepsilon} = f_2\left(\sigma_t, \dot{\bar{\varepsilon}}, T\right) \tag{2b}$$

$$\int_{\sigma_{t,initial}}^{\sigma_t} d\sigma_t = \int_0^{\bar{\varepsilon}} f_2\left(\sigma_t, \dot{\bar{\varepsilon}}, T\right) d\bar{\varepsilon} \tag{2c}$$

Two main structural obstacles to dislocation movement are recognized for polycrystalline OFHC copper. One is grain boundaries and the other is interaction between dislocations within a grain. In an early development of the MTS model for copper, based on experimental studies up to a strain ≈ 0.7, it is assumed that the grain boundary resistance to flow is constant during deformation, with negligible strain rate and temperature dependence [41]. Eq. 2a is developed to Eq. 3a, where σ_a is the grain boundary contribution to flow stress and s is an activation factor that takes a value between 0 and 1. It is recognized that, in a flow at constant $\dot{\bar{\varepsilon}}$ and T, structure will eventually reach a steady state, as the generation of dislocations (hardening) becomes balanced by their elimination (recovery). Then σ_t takes a saturation (maximum) value, written as η. It is found experimentally that Eq. 2b can be written as Eq. 3b, where θ is weakly dependent on $\dot{\bar{\varepsilon}}$ and η depends on $\dot{\bar{\varepsilon}}$ and T.

$$\bar{\sigma} = \sigma_a + s\left(\dot{\bar{\varepsilon}}, T\right)\sigma_t \tag{3a}$$

$$d\sigma_t/d\bar{\varepsilon} = \theta\left(\dot{\bar{\varepsilon}}\right) f\left(\sigma_t/\eta\right) \tag{3b}$$

The MTS model in this form has been applied to machining an annealed copper with a $\gamma = 30°$ tool [42]. Agreement is found between simulated and experimental results although it is only values of F_C and t/h that are compared.

An alternative but closely-linked physical model re-casts the structure and structure evolution equations directly in terms of dislocation density and structures. Greater complexity is introduced. The grain boundary contribution to flow stress becomes grain size, strain rate and temperature dependent, and grain size becomes strain dependent. The model formulation and application to copper machining is in [43,44]. Agreement is reported between simulated and experimental results in simulations with a $\gamma = 0°$ tool. In this case it is only values of F_C and F_T that are compared.

In the present paper it is the more simple approach [41] that is initially developed, with more detail later in this Introduction, then applied in Sections 3 and 4, before recognising the need to introduce aspects of the more complicated treatment in Section 5. Well-validated coefficients of this model are published and its simplicity helps attention to be focussed on the sliding friction modelling that is also needed for simulating chip formation.

13

Eq. 4 is the almost universally applied friction model. The Coulomb law $\tau_f = \mu_f \cdot \sigma_n$, with τ_f the friction stress, σ_n the normal stress and μ_f the sliding friction coefficient, acts unless τ_f becomes larger than the plastic shear stress of the chip material. Then τ_f becomes limited to the shear stress. This law reflects the physical conditions at the contact. Stresses are so large near to the cutting edge of the tool that a plastic state (secondary shear) arises. Towards the end of the contact, where the chip leaves the tool, the contact becomes elastic [45].

$$\tau_f = \min.\left(\mu_f \sigma_n, \bar{\sigma}/\sqrt{3}\right) \tag{4}$$

The question is what value of μ_f should be used in a simulation? One approach is to select the so-called apparent, or average, coefficient of friction, $\mu_f = \tan\lambda$, with λ determined from measured cutting and thrust forces (Eq.1). It is the approach taken in [42-44]. There are two problems with this. Fig. 2a shows an extremely wide measured range of λ. To select any one value alters a simulation from predictive to descriptive. It is useful (descriptive) for determining values of quantities not easily measurable, for example temperatures and stresses in the tool and cut surface, but is only valid once the appropriate value of λ is known (not predictive). The other problem is that if a simulation predicts cutting and thrust forces that agree with the measured values it implies that the friction law $\tau_f = \mu_f \sigma_n$ is active over most of the contact. It is not physically realistic.

The approach taken in this paper is to impose a value of μ_f so large that it forces the active friction law to be $\tau_f = \bar{\sigma}/\sqrt{3}$. Then λ predicted by the simulations becomes $< \tan^{-1}\mu_f$, dependant on the plasticity model. It is this paper's main original contribution as far as its modelling is concerned. Choosing $\mu_f > 1$ has been sufficient in previous works on the machining of steels, for example [46], and a Ti alloy [47]. It is an approximate way of ensuring secondary shear, because the elastic fraction of the contact is not exactly modelled, but it is certainly preferable to ignoring it.

Also the applied MTS model is updated from [41]'s original form. The original form of s in Eq. 3a is as in Eq. 5a. k_B is the Boltzmann constant, b the Burgers vector, g_0 is a normalized activation energy, μ_T is the elastic shear modulus at temperature T (with μ_0 the value at 0K), $\dot{\bar{\varepsilon}}_0$ is a reference strain rate and p and q are coefficients. The values of these quantities, from [41] and [50], are in Table 3. Subsequently an alternative form (Eq.5b) has been given [48]. It has the structure of the Zerilli-Armstrong activation function [49]. Its coefficients are also in Table 3. When the values for the constants in Table 3 are substituted respectively into Eqs. 5a and 5b, over the range of $\dot{\bar{\varepsilon}}$ and T that occur in machining ($\dot{\bar{\varepsilon}} \approx 500$ to 5E4/s, $T \approx 300$ to 550K), s is found to be the same from both

calculations to better than 2%. Eqs. 5a and 5b are numerically equivalent. Eq. 5b is preferred for the simulations to be reported in this paper.

$$s = \frac{\mu_T}{\mu_0} \left\{ 1 - \left[\frac{k_B T \ln\left(\dot{\bar{\varepsilon}}_0 / \dot{\bar{\varepsilon}}\right)}{g_0 \mu_T b^3} \right]^{1/q} \right\}^{1/p}$$ (5a)

$$s = \left(\mu_T / \mu_0\right) \exp\left[T\left(-C_3 + C_4 \ln \dot{\bar{\varepsilon}}\right) \right]$$ (5b)

Table 3. Values of the constants in Eqs. 5a and 5b. Data are from [41] and [48].
Additionally $\mu_T = \mu_0 (1 - 3.3\text{E-}4\text{K}^{-1})$ and $\mu_0 = 57\text{GPa}$ [50].

Eq.5a					Eq.5b	
k_B/b^3 (MPaK^{-1})	$\dot{\bar{\varepsilon}}_0$ (s^{-1})	g_0	q	p	C_3 (K^{-1})	C_4 (K^{-1})
0.823	10^7	1.6	1	2/3	3.6E-4	2.2E-5

The original form of Eq. 3b, appropriate for the Stage III strain hardening range of copper [51], is as in Eq. 6a, with expanded expressions for θ and η in Eq. 6b. Subsequent developments have occurred. Eq. 6c is the result, with Eq.6b unchanged. On the left hand side, $d\sigma_t$ and $d\bar{\varepsilon}$ are replaced by $d(\sigma_t/\eta)$ and $d(\bar{\varepsilon}/\eta)$. It is argued in [48] that integration of $d(\sigma_t/\eta)$ along a strain path leads to a more correct determination of σ_t when $\dot{\bar{\varepsilon}}$ and T vary along the path. An improved prediction of shape change in Taylor (projectile) impact tests supports this [52]. On the right hand side, a different form of Eq. 3b's f is introduced, justified both empirically [53] and physically [54]. The present paper adopts Eqs. 6b and 6c, with the constants, from [39], in Table 4 (k_B/b^3 and μ_T are as before). σ_a (Eq. 3a) is included for convenience.

$$d\sigma_t \Big/ d\bar{\varepsilon} = \theta\left(\dot{\bar{\varepsilon}}\right)\left[1 - \frac{\tanh\left(2\sigma_t/\eta\right)}{\tanh 2} \right]$$ (6a)

$$\theta = \theta_0 + \theta_1 \ln \dot{\bar{\varepsilon}} + \theta_2 \dot{\bar{\varepsilon}}, \quad \eta = k_0 \left(\frac{\dot{\bar{\varepsilon}}}{\dot{\bar{\varepsilon}}_{\eta,0}} \right)^{\frac{k_B T}{\mu_T b^3 A}}$$ (6b)

$$d\left(\sigma_t/\eta\right) \Big/ d\left(\bar{\varepsilon}/\eta\right) = \theta\left(\dot{\bar{\varepsilon}}\right)\left(1 - \sigma_t/\eta\right)^2$$ (6c)

Table 4. Further constants of the MTS model for OFHC copper. Values are from [41].

θ_0 (MPa)	θ_1 (MPa)	θ_2 (MPas^{-1})	k_0 (MPa)	$\dot{\bar{\varepsilon}}_{\eta,0}$ (s^{-1})	A (-)	σ_a (MPa)
2390	12	0.034	900	6.2E10	0.312	45

$\sigma_t = \eta$ in a completely saturated state. Then Eq. 3a becomes $\bar{\sigma} = \sigma_a + s\eta$. At a strain rate of 10^4/s and a temperature of 150°C, typical of primary shear, $s = 0.805$ and $\eta = 603$MPa are calculated from Eqs. 5b and 6b with constants from Tables 3 and 4. If a saturated state is reached in primary shear $k = \bar{\sigma}/\sqrt{3}$ = 306MPa. If the chip, without change of microstructure (η unchanged), is subsequently hardness tested ($HV \approx 3\bar{\sigma}$) at a strain rate of 10^{-2}/s at 20°C, $s = 0.789$ is obtained and $HV = 145$kg/mm^2. These values of k and HV are satisfyingly close to experimental values.

However when, in the present work, the plasticity and friction models reviewed in this Introduction are applied to simulating annealed copper chip formation, the simulated F_C* and t/h underestimate and F_T* overestimate experimental values by up to 20%. This is reported in Section 4. Speculative extensions of the plasticity model, to include Stage IV hardening and strain softening are introduced in Section 5 and are found to improve the simulations, respectively by increasing shear stress in the primary shear region and reducing the friction stress in the secondary shear region.

2. **Experimentation**

This paper's machining experimental arrangement is radial feeding a straight-edged tool into a rotating disc, also called plunge cutting. Copper discs are wire electro-discharge machined from round bars and mounted on a mandrel which is held in a lathe chuck to the left and supported by a revolving tail stock centre to the right. The discs are reduced from an outer diameter of 80-90mm (see Section 2.1) to an inner diameter of 50mm.

2.1. *The copper bar materials*.

Discs have been cut from two bars. One, of 89mm diameter, is grade C103/CW008A in an as-manufactured (hot extruded) state. The other, of 80mm diameter, is grade C110/CW009A supplied in a cold drawn state. Table 5 gives their certified data.

Table 5. CW008A and CW009A properties from their inspection certificates.

Designation	Mechanical properties				Composition[a] (Cu wt%, others ppm)				
	R_m (MPa)	$R_{p0.2}$ (MPa)	A5 (%)	HV10 (kg/mm^2)	Cu	Ag	O	Bi	Pb
CW008A	217	72	51	-	99.99	11	5	0.6	3.1
CW009A	313	306	15	102	99.998	9	1	< 1	< 0.7

[a]: CW009A composition, additional elements (ppm): As < 1, Cd < 1, Fe < 1, Mn 0.2, Ni < 1, P < 1, S 6, Sb < 1, Se 1, Sn < 1, Te < 2, Zn < 1.

Vickers hardness testing with a 10kg load shows a uniform hardness across diameters (Fig. 4a). Annealing trials at 300ºC carried out on the CW009A material show softening to occur after 2hrs (Fig. 4b). Machining tests have been carried out on the three materials: CW008A as received, CW009A as received and CW009A after 2hrs annealing at 300ºC.
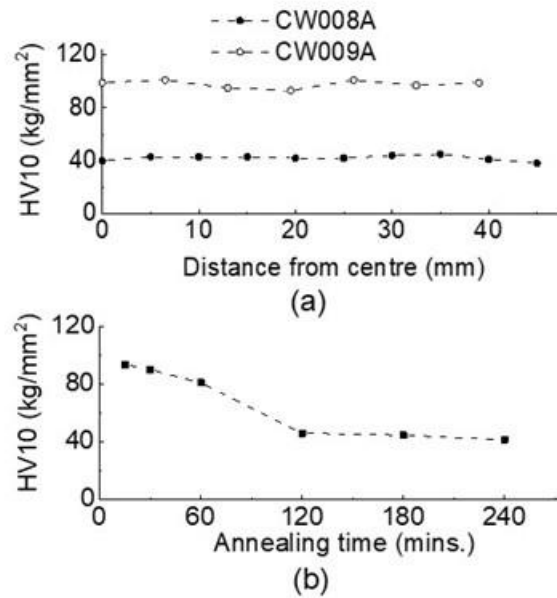

Fig. 4. Vickers hardness values of the copper bars. (a) Across the diameters of CW008A and CW009A bars as received. (b) Against time for annealing CW009A as received at 300°C.

Fig. 5 shows the microstructures of all three. Their room temperature and low strain rate (10^{-3}/s) strain hardening behaviours, measured by simple compression of cylinders initially 9mm high and 6mm diameter, are in Fig. 6. The cylinders were placed between platens in a sub-press and compressed in three stages, 2.25mm at a time, by a 100kN capacity Instron 4206 test machine. Between each stage the cylinder/platen contact was sprayed with a PTFE based lubricant. It was judged that friction has a negligible influence on loading up to a strain ≈ 0.6.

Fig. 6 also includes the strain hardening predicted from Section 1's MTS model with constants from Tables 3 and 4 (see Appendix A1 for the derivation). $(\sigma_t/\eta)_{initial}$ (Eq.2c) is chosen to be 0.1. Clearly no one model fits all three coppers. The chosen model is a good fit for the CW008A copper.
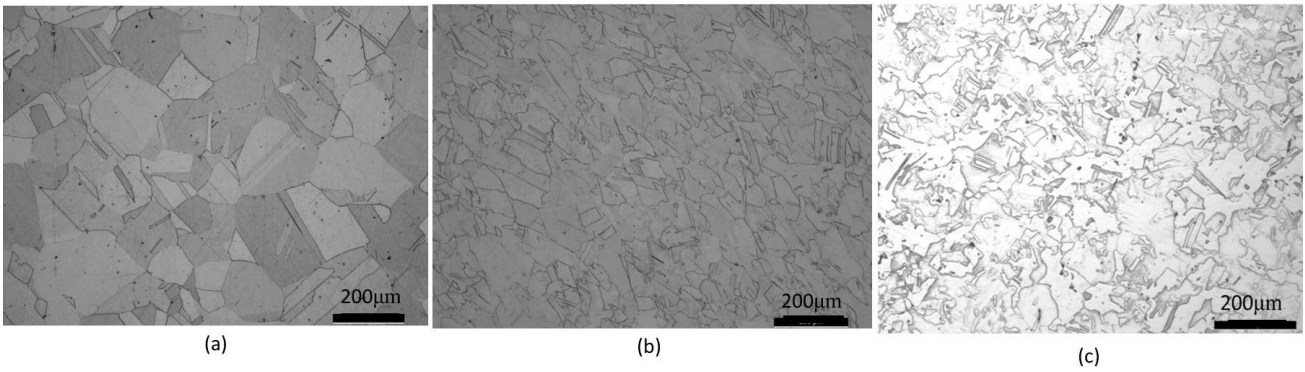
Fig. 5. Microstructures of the copper bars. (a) CW008A as received. (b) CW009A as received. (c) CW009A after annealing for 2hrs at 300°C. In all cases the etchant is 50ml HNO$_3$ + 50ml H$_2$O.
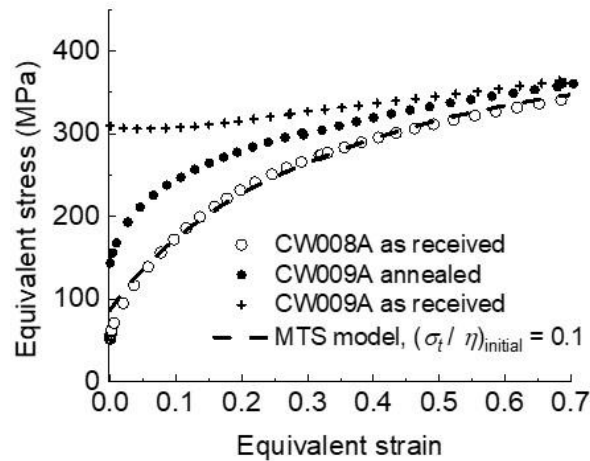

Fig. 6. Strain hardening of the copper materials. The figure compares the experimental results for CW008A as received, CW009A as received and CW009A annealed with the predictions from the MTS model with Table 3 and 4 coefficients. Test conditions are room temperature and a strain rate of 10^{-3}/s.

2.2. *The cutting tool inserts*.

The cutting tools used in this project are inserts obtained from a single source [55] and held in a standard holder. The inserts are listed in Table 6. The rake angles γ are the true angles measured with the holder in position. The clearance angles α are nominal values. The inserts, chosen for their rake and clearance angles and cutting edge radii r_β, but limited by their availability ($\gamma = 8\text{-}25°$ is the available range), have different substrates (carbide and high speed steel) and coatings (TiN, TiAlN, AlCrN and uncoated). The room temperature thermal conductivities of the carbide and high speed steel are 87 and 27W/mK respectively, from supplier information. The main test program uses the γ = 8 and 19° coated inserts, chosen as representative low and high rake angle inserts. The γ = 12° insert and the 19° uncoated insert are used in subsidiary tests (Section 2.3).

18

Table 6. Insert designations with their source, materials and geometry. γ are measured values with the insert in position. α are nominal values. r_β are measured values with ranges from two inserts.

Designation and source		Materials		Geometry		
ISO code	Source	Substrate	Coating	γ(°)	α(°)	r_β(µm)
APFT 16 04 PD FR-111	Alesa	Carbide	TiAlN	8	11	17±1
APFT 16 04 08 FR-121	Alesa	Carbide	AlCrN	12	11	11±2
APFT 16 04 04 FR	Alesa	HSS	TiN	19	11	11±2
APFT 16 04 PD	Alesa	HSS	Uncoated	19	11	13±2

2.3. *The machining conditions*.

The initial plan was to machine at a range of cutting speeds (v_c from 5 to 300m/min) at a fixed uncut chip thickness $h = 0.13$mm (feed of 0.13mm/rev), considering the conditions in Table 1, choosing the copper disc width $w = 6$mm to ensure plane strain conditions. However at low speeds the Kistler force measurement platform (Section 2.4) became overloaded. Subsequently h was reduced to 0.08mm. Further, a disc was completely consumed at $v_c = 300$m/min by machining for long enough to establish a thermal steady state. The maximum v_c was reduced to 200m/min. Table 7 summarises the main test conditions, all with coated inserts (the measured disc width ranged from 6 to 6.2mm). It also lists subsidiary tests. Those with the $\gamma = 12°$ AlCrN coated insert and the 19° uncoated insert were carried out to extend the range of chip / tool material contact conditions. In addition the tests with the 19° uncoated insert, and with the 8° insert with $w = 2$mm, were carried out to create process conditions closer to those in the earlier work (Table 1), in which all tools were HSS and in which, in some cases, low values of the ratio w/h led to large departures from plane strain. All tests were in air, without cutting fluid.

Table 7. Cutting test conditions. $h= 0.08$mm, $v_c = 5$-200m/min, $w = 6$mm unless otherwise stated.

Series	Main			Subsidiary		
Work material	CW009A as received	CW009A annealed	CW008A as received	CW008A as received	CW008A as received	CW008A as received
Insert γ (°)	8[a], 19[a]	8[b], 19	8[c], 19	12	19 uncoated	8[d]

[a]: also $h = 0.13$mm, min.$v_c = 10$m/min for $\gamma = 8°$; [b]: max.$v_c = 300$m/min; [c]: min.$v_c = 50$m/min; [d]: $w = 2$mm.

The cut time for tests at $v_c \geq 25$m/min was 5s, required to reach a thermal steady state, but for $v_c = 10$ and 5m/min cut time was increased to that required for ≈ 10 revolutions of the disc (≈ 10 and 20s respectively). Tests were systematically repeated at $v_c = 50$m/min to assess whether there was any variation of chip formation across the disc diameter and whether there was any effect of cut distance (tool wear or perhaps some other form of edge conditioning). The cutting edge was changed if tool

wear was suspected and whenever unexpected behaviour occurred that might have been due to wear (unchanged chip formation on changing the edge was taken to discount the possibility).

2.4. *Measurement methods*.

Cutting and thrust forces were measured by a Kistler force platform (type 9121) on which the tool holder was mounted. Chips were collected and their widths *w* measured with a vernier caliper. A mean effective chip thickness was determined by weighing measured chip lengths. For this it was assumed that the thickness is constant across the chip width, that the cut chip width is the same as the uncut width and that the density of copper is $8.96g/cm^3$.

Selected chips were sectioned and mounted for metallographic examination. The section Vickers hardness was measured at 0.1kg load. Vickers hardness testing, also at 0.1kg load, was further carried out directly on the back faces of chips. These were smooth enough from sliding over the tool not to require any particular preparation.

The Vickers hardness distributions beneath cut surfaces from tests at $v_c = 5$ and 100m/min, were measured, also at 0.1kg load, on sections cut back and polished 2mm from the disc side face. These sections were also examined metallographically by etching. Cut surface texture was imaged optically, both qualitatively using a digital inspection microscope (Leica DMS1000) and quantitatively with a focus variation instrument (Alicona IFG4). Cutting was stopped at 5m/min by applying the lathe's emergency brake. At 100m/min, a rapid axial feed was applied to the tool without stopping the radial feed or disc rotation. The insert cleared the disc within 3 revolutions, leaving a 2mm pitch, 0.08mm stepped, spiral on the disc's cylindrical face.

3. Model implementation and simulation conditions

The MTS model (Eqs. 3a, 5b, 6b and 6c), with the constants from Tables 3 and 4, and the friction law Eq.4 with $\mu_f = 2.0$, is implemented in a time-stepping manner, as a user-defined sub-routine, in the commercial finite element code AdvantEdge2Dv7.5. It is an explicit dynamic Lagrangian software bespoke for simulating chip formation in metal cutting, developed from [56]. Its particular value for the present work is its adaptive meshing and re-meshing capability designed for the chip formation geometry, and for the detail of its friction law. This can cope with high values of μ_f. $\mu_f = 2.0$ is found in the present case to be necessary to enforce $\tau_f = \bar{\sigma}/\sqrt{3}$, activating secondary shear at the chip / tool contact. Also the value of $\bar{\sigma}$ in the friction law is the local value at the contact, dependent in this case on the local micro-structure and varying from place to place in the contact (some codes require $\bar{\sigma}$ to be input as a nominal value).

The time-stepping routine is outlined in Eq. 7. It is the incremental form of Eq. 6c. With σ_t, η and $\bar{\varepsilon}$ known at time step (n – 1), θ varying only slightly with strain rate and δt being the time step duration, σ_t/η at time step n is obtained from that at step (n-1), with $\bar{\varepsilon}_n$ obtained from $\bar{\varepsilon}_{n-1}$ by $\bar{\varepsilon}_n = \left(\bar{\varepsilon}_{n-1} + \dot{\bar{\varepsilon}}\delta t\right)$. Finally $\sigma_{t,n}$ is obtained from the product of $(\sigma_t/\eta)_n$ and η_n; and $\bar{\sigma}$ is obtained from Eqs. 3a and 5b. More detail is in Appendix A2.

$$\left(\sigma_t/\eta\right)_n = \left(\sigma_t/\eta\right)_{n-1} + \theta\left(1 - \left(\sigma_t/\eta\right)_{n-1}\right)^2\left[\left(\bar{\varepsilon}/\eta\right)_n - \left(\bar{\varepsilon}/\eta\right)_{n-1}\right] \tag{7}$$

The validity of this simulation scheme is checked by room temperature tensile test simulations at strain rates from 10^{-3} to 10^5/s. Details are in Appendix A3.

The modelling is applied to simulations of chip formation for two rake angles $\gamma = 8$ and $19°$ and cutting speeds v_c from 5 to 200m/min, with $h = 0.08$mm, to match experimental conditions. The tool thermal conductivity is chosen to be 87W/mK for $\gamma = 8°$ and 27W/mK for $\gamma = 19°$, also to match the experimental conditions, but no account is taken of the tool coatings. Tool heat capacity is given the artificially low value of 10^3J/kgK. This reduces the time (cut distance) required to reach a steady state temperature distribution at the rake face [57]. The thermal conductivity and heat capacity of the copper work material are taken to be 400W/mK and 3.45MJ/m³K, independent of temperature. The work material is arbitrarily given a near-annealed initial state of $(\sigma_t/\eta) = 0.1$. The low strain rate, room temperature, strain hardening curve with this choice is in Fig. 6.

The default choice of tool cutting edge radius r_β is 20μm. It is slightly larger than the new insert values of 17μm ($\gamma = 8°$) and 11-13μm ($\gamma = 19°$) but a measurement in Section 4 shows r_β of a 19° insert to increase by 7μm after use. In one circumstance ($\gamma = 8°$, $v_c \leq 50$m/min) r_β is chosen to be 30μm for computation time reasons. Consideration of the influence of edge radius (ploughing) on predicted cutting forces is in Appendix B1, with time consequences from edge radius and meshing choices in Appendix B2.

The software is used in its 'High Performance Machining' mode. This allows multiple passes to be taken, with the cut surface state from one pass preserved for the next pass. Three passes are chosen in this work. It is found necessary to vary the workpiece meshing strategy, in various minor ways, from one simulation to another. More detail is in Appendix B2 but in general the minimum mesh size is chosen between ¼ and ½ of the tool edge radius. Fig. 7a is an overview of a typical mesh of minimum size 10μm. The cut surface maintains a fine mesh to a depth $\approx 4h$. Fig. 7b shows the primary shear region at greater magnification.

Example chip formation predictions are shown in Fig. 8. 1st pass chips are always thickest, 2nd pass chips thinnest and 3rd pass chips take an intermediate value (in this case t/h = 9.6, 3.1 and 5.1 respectively). The figure also shows contour plots of temperature, strain rate and strain. In particular (b) demonstrates plastic shear in the secondary shear region, (c) shows both a high strain in the chip next to the rake face, due to the secondary shear, and a high strain at the free surface, due to strain in the cut surface from the previous pass. In (c) the strain in the cut surface before the cut is the same as in the new surface after the cut. It demonstrates that a steady state is reached.

Example cutting and thrust force dependences on cut distance are in Fig. 9. The cut distance to reach a steady state for the 1st pass increases with t/h. Fig.9 is an extreme example, with v_c = 5m/min. At the 2nd pass forces typical pass through a maximum before settling down to a steady state. In this example it is because cut surface strain hardening is not initially developed. At higher cutting speeds it is additionally because, at the start of cut, rake temperature increases with cut distance and friction stress reduces. At the 3rd pass a steady state is reached at the least cut distance.

In all cases, forces are extracted from the steady state region of outputs such as in Fig. 9. t/h is measured directly from contour plots. Required cut distances vary from 10-12mm at v_c = 5m/min to 6mm at v_c = 200m/min, with elapsed computing times from $\approx$ 12 to 4 days (with 8 core parallel computation and a CPU clock rate of 3.7GHz): see also Appendix B2.
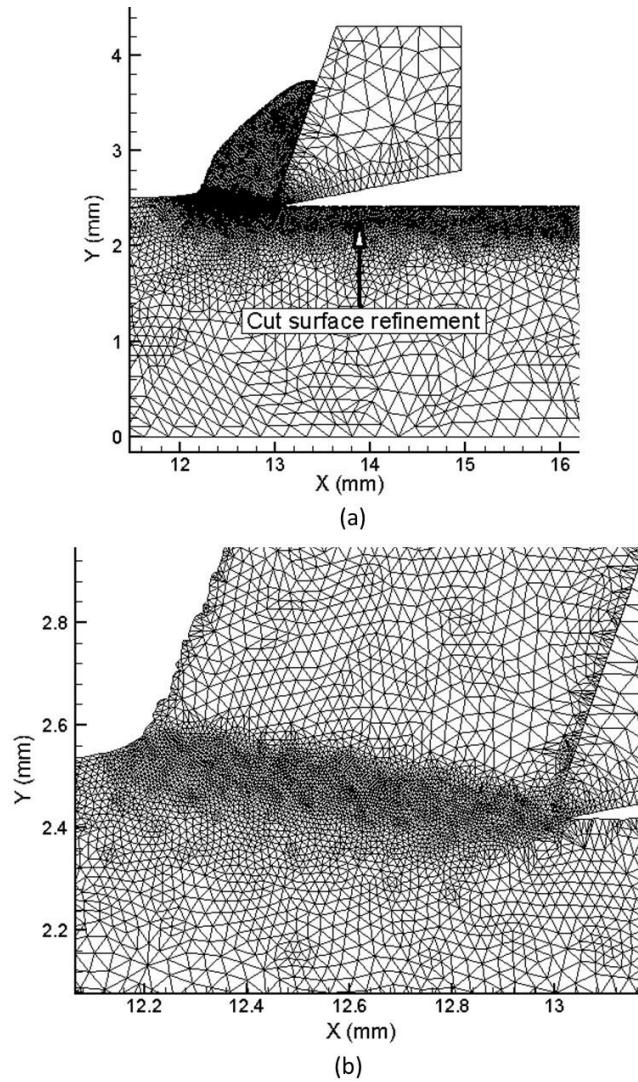
Fig. 7. A typical simulation mesh. (a) A general view. (b) At a higher magnification. The purposes are to show (a) the depth of mesh refinement below the cut surface and (b) refinement in the chip formation region. This example is from a 1st pass simulation with $\gamma = 19°$ and $v_c = 50\text{m/min}$.
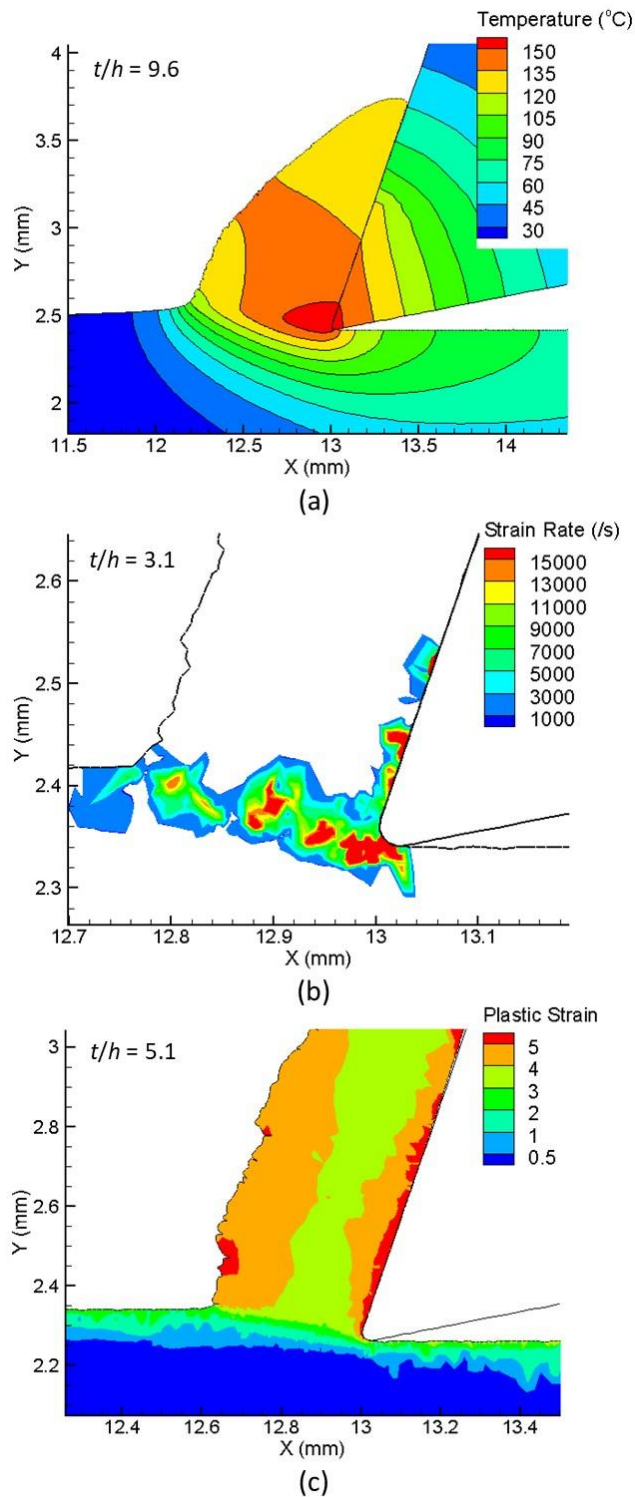
Fig. 8. Examples of simulated chip formation with contour plots. (a) A 1st pass simulation with temperature contours. (b) A 2nd pass simulation with strain rate contours. (c). A 3rd pass simulation with strain contours. Each pass generates a different value of *t/h*, as marked. Each part is at a different magnification to compensate for the different *t/h* values. (a) shows a maximum temperature close to the cutting edge. In (b) the high strain rate next to the rake face demonstrates that secondary shear occurs. (c) shows a high strain in the cut surface ahead of the tool from the previous pass. In this example $\gamma = 19°$, $v_c = 50$m/min and $h = 0.08$mm.
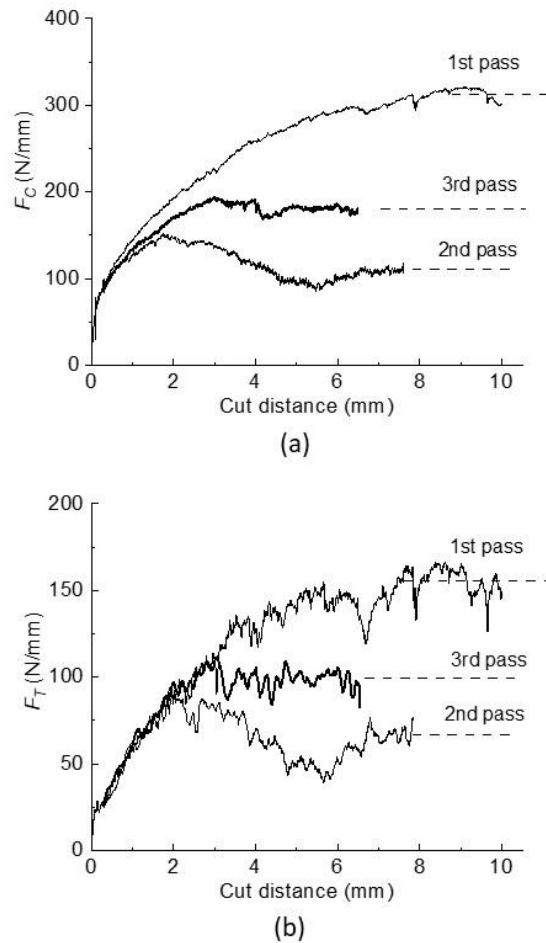
Fig. 9. Force increases at start of cut. (a) F_C dependence on cut distance and pass. (b) F_T dependence on cut distance and pass. In both (a) and (b) the distance to reach a steady state is greatest for the 1st pass and least for the 3rd pass. In this example $\gamma = 19°$, $v_c = 5$m/min and $h = 0.08$mm.

4. Experimental and simulation results

Section 4.1 contains general experimental observations. Experimentally measured F_C, F_T and t/h are compared with predictions from simulations in Section 4.2. Hardness testing results, cut surface observations, and simulations of conditions below the cut surface are in Section 4.3.

4.1. *General observations*.

Chip width measurements. Chip width measurements when $w = 6$mm show < 10% increase over uncut widths with $\gamma = 19°$ inserts but up to 20% increase at low cutting speeds with $\gamma = 8°$ inserts. Plane strain conditions (i.e. uniform chip thickness) exist over more than 80% of the chip width. Reducing w to 2mm causes a large chip side spread, depending on v_c: at $v_c = 5$, 10, 25, 50, 100 and 200m/min measured chip widths are respectively ≈ 4.1, 3.6, 3.4, 3.1, 2.7 and 2.5mm.

25

Force and t/h increase with insert use. In a first set of tests (CW009A as received, $\gamma = 19°$, $h =$ 0.13mm) a disc was reduced from its external to internal diameter by machining with a single cutting edge consecutively at cutting speeds 50, 100, 50, 10 and 50m/min again. 50m/min was then repeated at the external diameter of a second disc before changing to a new edge and machining again at 50m/min. Fig. 10 shows F_C*, F_T* and t/h measured during each of the $v_c = 50$m/min periods. The steady increase of all these with cut distance, with no jump on changing from the first to the second disc; and the return to the original levels on changing to a new cutting edge, shows that the changes are due to some changing tool edge or rake face condition rather than due to any influence of diameter at which a cut is taken (transfer of copper to the tool faces did not occur and there was no flank wear; an increased edge radius of 17-20µm was measured but it is not clear that this can explain the force and chip thickness increase). In this case F_C* and F_T* increased by 0.35GPa and 0.22GPa respectively and t/h by 1.0 during the edge's use. Subsequently, with edges changed at least once per disc, and with test repetition spot checks, increases in F_C* and F_T* due to edge use have been held to < 0.3GPa and < 0.2GPa respectively and in t/h to < 1. These set the levels of uncertainty in the data to be reported.

26
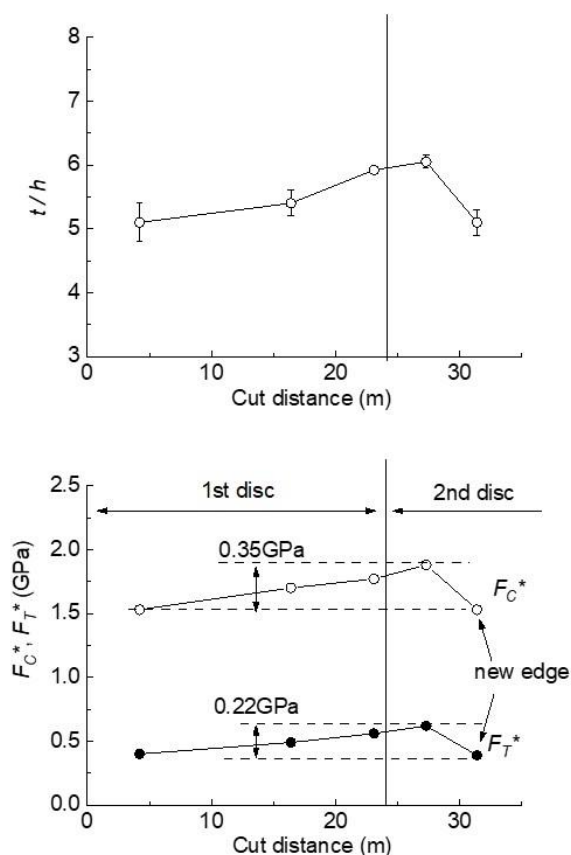
Fig. 10. Changes in F_C*, F_T* and *t/h* with insert use. F_C*, F_T* and *t/h* increase steadily with cut distance, even as a 1ˢᵗ disc is completely used up and replaced by a 2ⁿᵈ disc at the distance ≈ 24m. Replacing the insert by a new edge at the cut distance ≈ 30m results in F_C*, F_T* and *t/h* regaining their original values. It demonstrates that the changes are not due to the diameter at which the cut is being taken but due to insert degradation with use. This example is for cutting CW009A copper as received, with γ = 19º, *h* = 0.13mm and v_c = 50m/min. The uncertainty limits in *t/h* are ranges from three repeat measurements.

Types of chip formation. Chip formation is qualitatively the same for all three copper materials. Three situations occur depending on cutting speed.

At v_c = 5 and 10m/min cutting and thrust forces are high throughout one revolution of the disc, then low over the next. This cycle continues throughout the test as seen in Fig. 11a. The chip formed in each cycle is correspondingly thick and thin (Fig. 11b): in this case the cross-section area of the thick length is estimated to be ≈ 11mm², close to that of 13mm² expected from one revolution of the disc. Figs. 11c-d are respectively larger magnification views of the thin and thick chip sections. Chip thickness ratios *t/h* are deduced of ≈ 2.8 and 14. Parts (a-c) are from machining annealed CW009A copper. Parts (d-e) are for machining CW008A. This copper shows an extreme cyclical behaviour, with *t/h* often but not always reaching 20-25 during thick chip formation (Figs. 11d,e).

The speed range v_c = 25 to 50m/min is a transition range. Forces still show cyclic variation (Fig. 12a) but with much reduced regularity. Cycles are no longer clearly related to the number of disc revolutions. Chip thickness oscillates also less regularly. A plan view of the free surface of the chip shows thickness to vary across the chip width: it leads to a snaking of the chip along its length. Fig. 12b shows a chip macro-section. Figs. 12c-d are at larger magnification. Local chip thickness ratio swings between ≈ 6 and 11. The snaking occurs in the tests with *w* = 6mm. A different behaviour occurs when *w* = 2mm. This is introduced in the text around Fig. 17.

At speeds v_c ≥ 100m/min chip formation becomes steady, judged by the cutting and thrust forces. Fig. 13a shows forces at v_c = 200m/min. They reduce to a steady value with increasing time, generally considered to be the time required for the tool rake surface to heat to a steady temperature. Chip sections are steady at v_c = 100m/min (Figs. 13b-c) but at v_c = 200m/min minor periodic thickness variation can be seen by eye (Fig. 13d). Larger magnification (Fig. 13e) shows this to be a wavy rather than a saw tooth form. Whether it is a material or a machine tool effect has not been investigated. The wrinkled free surface remains at both speeds (Figs. 13c,f).
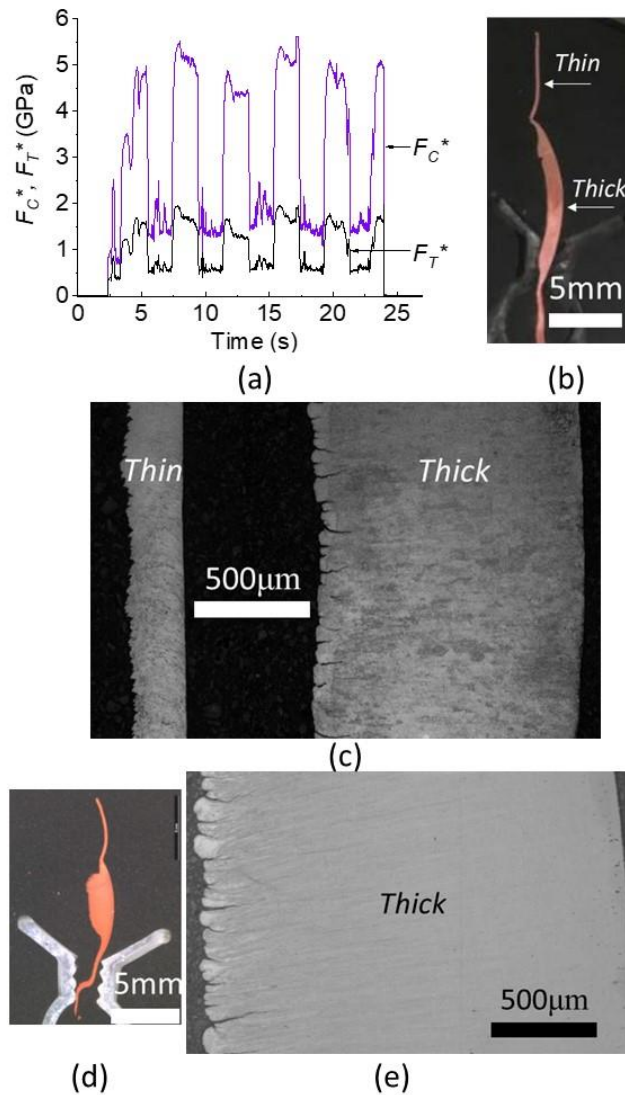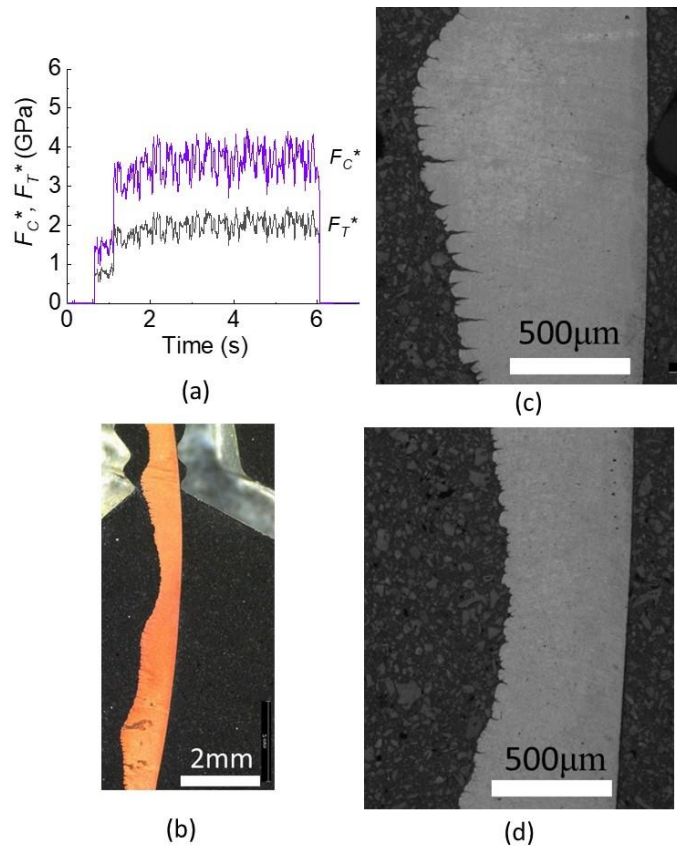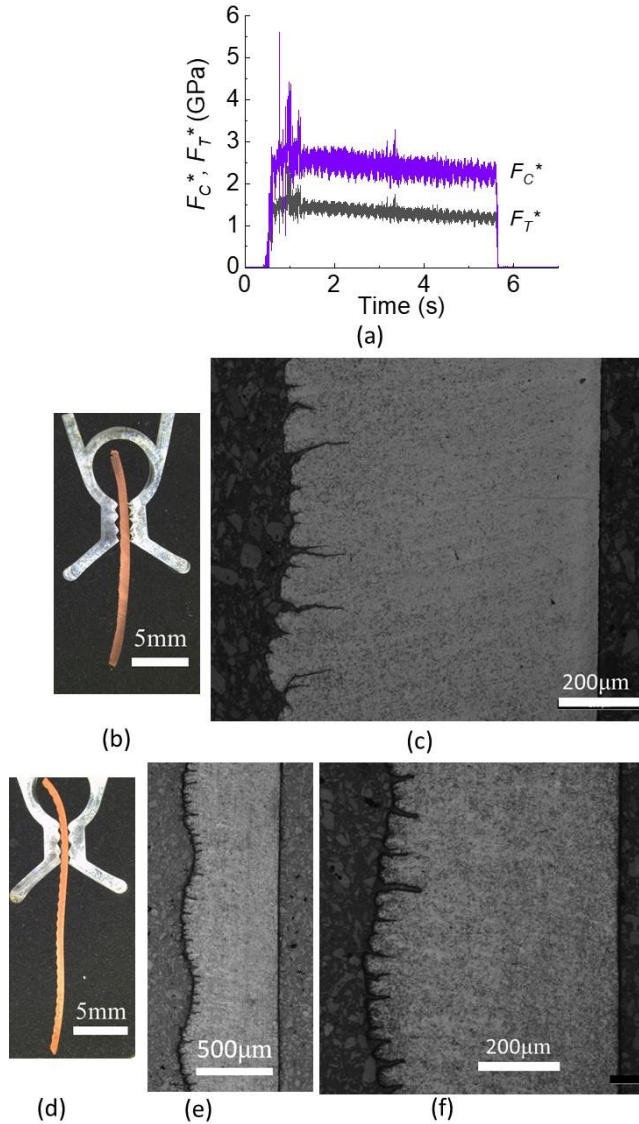
Fig. 11. Chip formation characteristics at cutting speeds 5 to 10m/min.: (a) F_C* and F_T* variation with cut time for a test lasting for 11 disc revolutions, showing cyclical force generation. (b) A chip section macro-view showing thin and thick formation phases. (c) Higher magnification thin and thick section views from which t/h = 2.8 and 14 can be estimated. (a to c) are from machining annealed CW009A copper. (d) A macro view for CW008A copper. (e) A thick section micro view for CW008A copper. For this extreme example t/h = 23. All these cases are from tests with γ = 19°, h = 0.08mm and v_c = 5m/min. In part (a) different colours are given to F_C* and F_T* to aid the eye. This colour code is repeated in Figs. 12 and 13.

Fig. 12. **Chip formation characteristics at cutting speeds 25 to 50m/min**. (a) F_C^* and F_T^* variation with cut time for a test lasting for 10.6 disc revolutions, showing less regular force oscillations than in Fig. 11a. (b) A chip section macro-view, showing less regular thickness oscillations. (c) and (d) micro-sections showing varying chip thickness, with t/h from ≈ 11 to 6. All these cases are from tests with CW009A copper as received and $\gamma = 8°$, $h = 0.08$mm and $v_c = 25$m/min.

Fig. 13. **Chip formation characteristics at cutting speeds 100 to 200m/min**. (a) Specific force variation with cut time for a test lasting for 66 disc revolutions. Forces reduce to a steady state with time (v_c = 200m/min, CW008A copper). (b-c) Chip section macro- and micro-views (v_c = 100m/min, CW008A copper, t/h = 9). (d-f) Chip section macro- and micro-views (v_c = 200m/min, annealed CW009A, $t/h \approx 7$). In all cases h = 0.08mm, γ = 8°.

4.2. *Force and chip thickness ratio detailed observations*.

Here and in following sections graphical results are colour coded for clarity. Experimental results from the main test series with γ = 19° inserts are coloured red. Those with 8° inserts are coloured blue. Results from the additional tests are coloured black. Results from simulations are coloured orange.

The observed reductions of F_C^*, F_T^* and t/h with increasing v_c for chip formation with γ = 19° inserts are recorded in Figs. 14 and 15.

In Fig. 14 the cyclical values at v_c = 5 and 10m/min are averaged. No significant difference is seen between any of the main test results. Although the forces from the CW009A as received tests with h = 0.08mm are systematically lower bounds to the others, they depart from them by less than the uncertainty ranges of 0.35 and 0.22 GPa from Fig. 10. Only the results from the uncoated tool tests are significantly lower than the others, both in their force and t/h values.
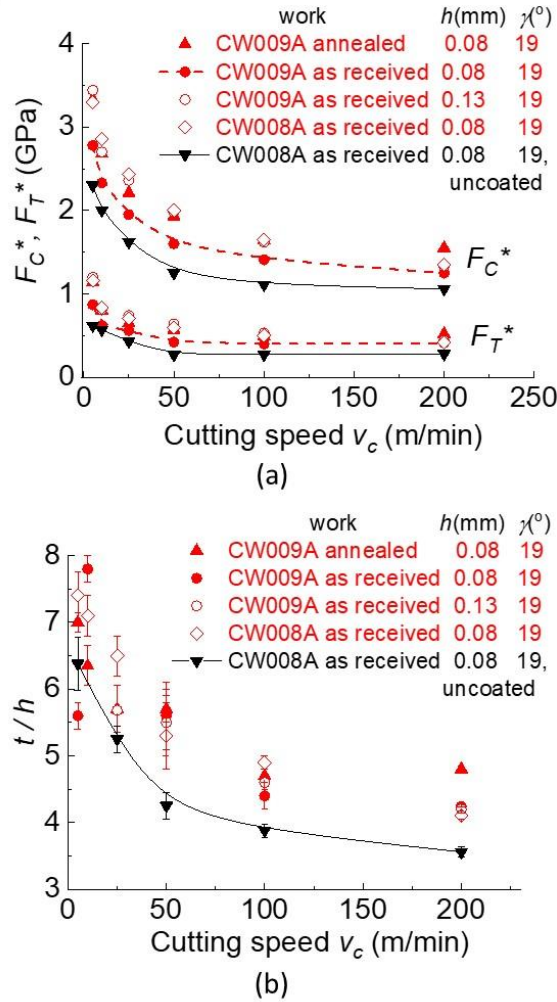

Fig. 14. Measured forces and chip thickness ratios for $\gamma = 19°$ inserts. (a) F_C* and F_T* and (b) t/h dependence on v_c. The results at v_c = 5 and 10m/min are averages from high and low cyclical values. The values from the main test program are colour coded red and from the subsidiary program are colour coded black (Table 7).

Fig. 15 selects the h = 0.08mm, $\gamma = 19°$ main test results and compares them with predictions from the simulations, including the low speed cyclical behaviour. The uncoated tool results are considered further in Section 5. The results from 1st and 2nd pass simulations at v_c = 5m/min are in approximate agreement respectively with the high and low cyclical experimental results at v_c = 5 and 10m/min (excluding the extreme behaviour of Fig. 11e). For $v_c \geq 25$m/min, the simulated 3rd pass (steady

31

state) F_C* and t/h results lie below the experimental results by ≈ 10-20% and the simulated 3rd pass F_T* are too large by ≈ 20%.
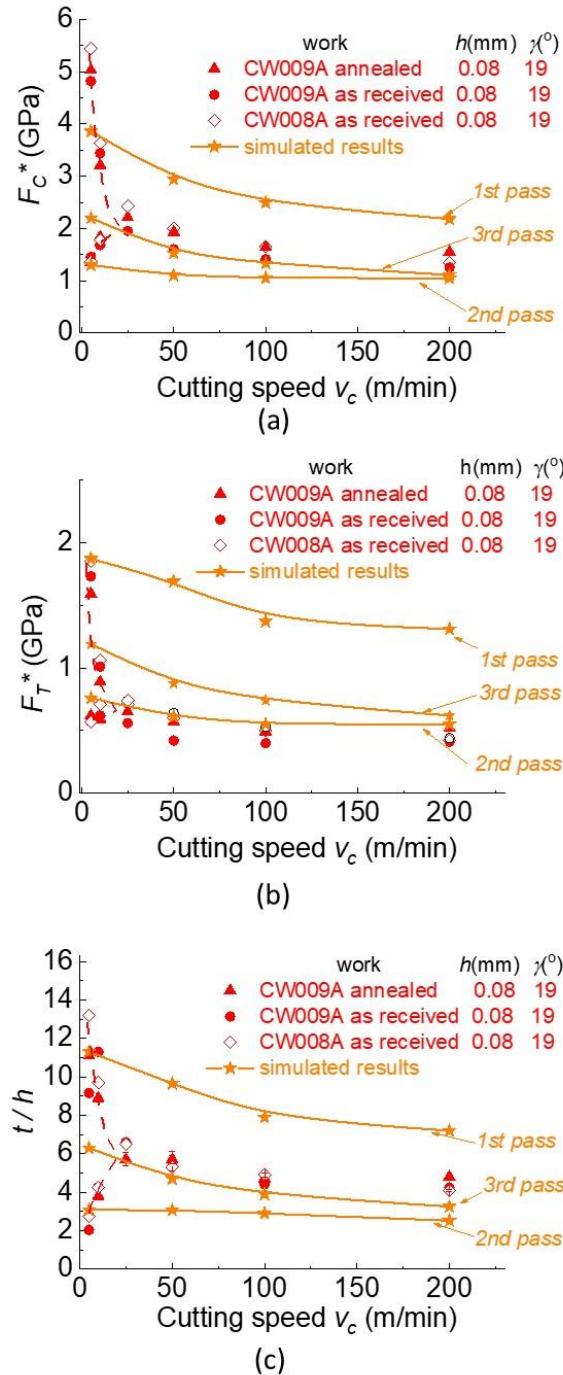

Fig. 15. Comparisons of experimental and simulated results for γ = 19° inserts. (a) F_C*, (b) F_T*, and (c) t/h dependence on v_c. The experimental results at v_c = 5and 10m/min include the low speed cyclical behaviour. The experimental results are colour coded red, with the dashed red lines guiding the eye. The simulated results are colour coded orange and show the different values from 1st, 2nd and 3rd passes.

Figs. 16 and 17 repeat Figs. 14 and 15 but for γ = 8° inserts (in one case γ = 12°). In Fig. 16 no significant difference is seen between any of the main test results except that F_C* and F_T* are lower

when $h = 0.13$mm. F_C^*, F_T^* and t/h are also lower when $\gamma = 12°$. Reducing w to 2mm does not alter F_C^* and F_T^*, nor t/h (with t/h determined from chip weight per unit length).
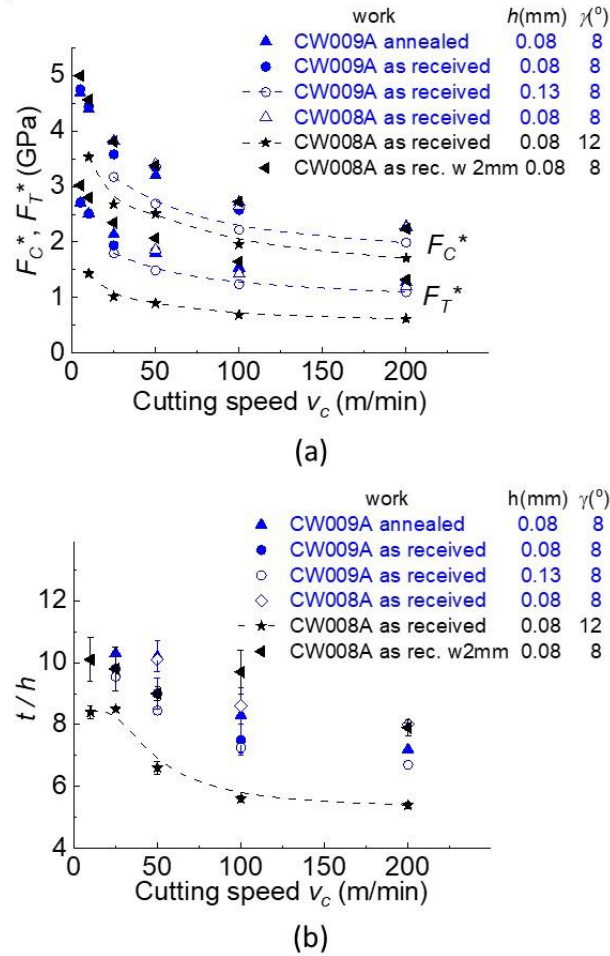
Fig. 16. Measured forces and chip thickness ratios for $\gamma = 8$ and $12°$ inserts. (a) F_C^* and F_T^* and (b) t/h dependence on v_c. The results at $v_c = 5$ and 10m/min are averages from high and low cyclical values. The values from the main test program are colour coded blue and from the subsidiary program are colour coded black (Table 7).

Fig. 17 compares selected experimental results (those from the main tests with CW009A, both annealed and as received, with $h = 0.08$mm and $\gamma = 8°$, and also from the additional tests with CW008A and $w = 2$mm) with the simulated results. The cyclical chip formation observations are included. The results from the $\gamma = 12°$ tests are considered further in Section 5.

The observed cyclical chip formation is more diverse than with the $\gamma = 19°$ tests. When $w = 2$mm chip thickness remains constant across the chip width in the transition range $v_c = 25\text{-}50$m/min (unlike with $w = 6$mm, see Section 4.1). It becomes possible to follow, up to $v_c = 100$m/min, the reducing cyclical amplitude with increasing v_c of all of F_C^*, F_T^* and t/h (in this case alone t for the thick chips is determined by micrometer). Fig. 17 shows two cyclical chip formation ranges, up to $v_c = 25$m/min for $w = 6$mm, and up to 100m/min for $w = 2$mm.

33

It is no longer the case that the results from 1st and 2nd pass simulations are in agreement respectively with the high and low cyclical experimental results at v_c = 5-10m/min. However for $v_c \geq$ 100m/min and at all speeds when average values are considered, the simulated 3rd pass (steady state) results lie below the experimental F_C* and t/h by $\approx 20\%$ and lie above the experimental F_T* by $\approx$ 15%. These values are similar to those from the γ = 19° tests.
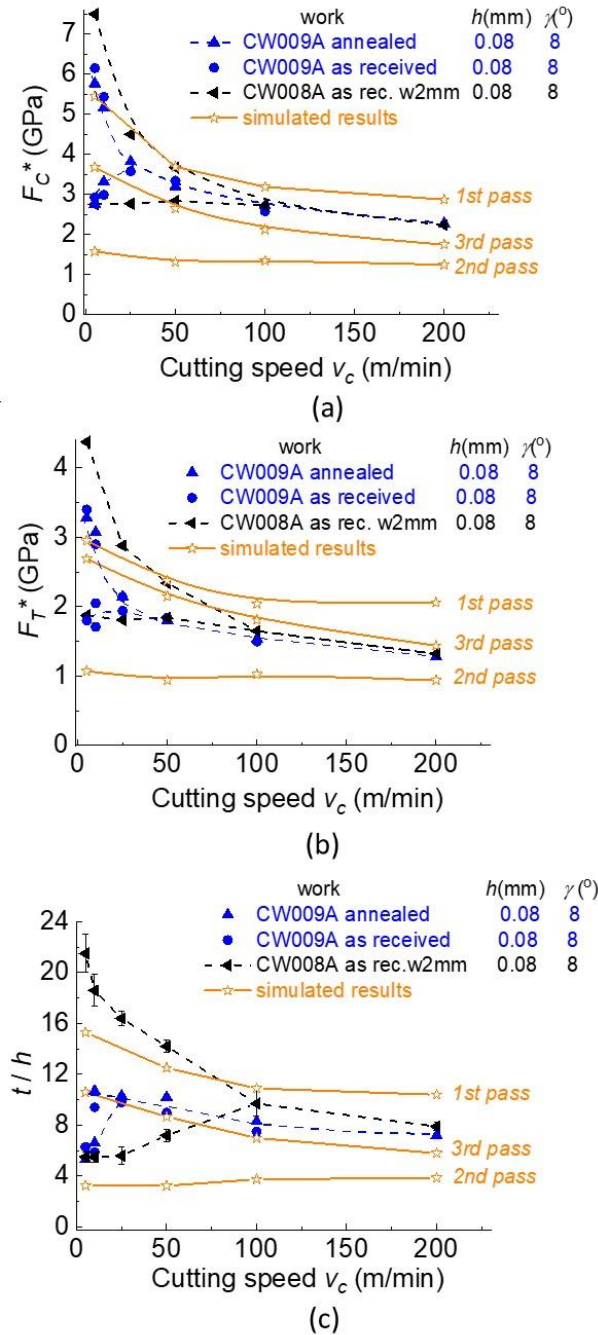

(a)

(b)

(c)

Fig. 17. Comparisons of experimental and simulated results for γ = 8° inserts. (a) F_C*, (b) F_T*, and (c) t/h dependence on v_c. The experimental results include the low speed cyclical behaviour, at v_c = 5and 10m/min in the case that w = 6mm and up to 100m/min when w = 2mm. The experimental results are colour coded blue and black (respectively for the main and subsidiary test programs), with

the dashed lines guiding the eye. The simulated results are colour coded orange and show the different values from 1st, 2nd and 3rd passes.

4.3. *Hardness and cut surface observations*.

Vickers hardness measurements from sectioned and polished chips (and from the chips' backs) are collected in Table 8. The major reduction in hardness as v_c increases from 5 to 25m/min is in accord with chip formation changing from region I/II to III or IV (Fig.3 [19]). Over the same speed range hardness values obtained from the backs of chips change from less than to greater than those from the chip bulks.

Table 8. Chips' Vickers hardness. The uncertainties in hardness are ranges from at least 3 measurements.

Material	γ (°)	v_c (m/min)	HV0.1(kg/mm²) Chip bulk	Chip back
CW009A as received	19	5	139 ± 2	132 ± 2
CW008A as received	19	5	143 ± 2	136 ± 2
CW009A as received	8	25	79 ± 4	86 ± 2
CW008A as received	8	100	79 ± 4	85 ± 5
CW009A annealed	8	200	72 ± 2	78 ± 2
CW009A as received	19	200	96 ± 1	101 ± 1

Measured hardness distributions below selected cut surfaces are shown in Fig. 18. The work material is CW008A as received in parts (a) and (b) and CW009A as received in part (c). Simulated strain and hardness distributions are included in parts (a) and (b). Simulated hardness is obtained from simulated strain by means of the empirical formula Eq.8, from [58]. It is calibrated over the range $\bar{\varepsilon} = 0.01$-1.0 by Vickers hardness tests on initially annealed C101/CW004A grade copper ($HV = 50$-55kg/mm²) strained in compression. In Figs. 18a,b simulated HV is only included from the calibrated range. Simulated strain and hardness values are not included in part (c) because the strain hardening curve of as CW009A as received (Fig. 6) does not follow that assumed for the MTS model.

$$HV\left(kg/mm^2\right)=132\bar{\varepsilon}^{0.197}$$ (8)

Fig. 18a is from a condition of cyclical chip formation. It records experimental hardness profiles measured after both thick and thin chip cycles and all of 1st, 2nd and 3rd pass simulated predictions. There is no significant difference between hardness distributions after thick and thin chip formation, nor much difference between simulated 1st, 2nd and 3rd pass simulations. Qualitative judgement of

how deep is the deformed layer would vary from $d/h \approx 20$ from HV values, to $d/h \approx 10$ from simulated HV values, perhaps to $d/h < 4$-8 from simulated strain values.

Fig. 18b is from a condition of steady chip formation. Only the 3rd pass simulated result is included. In this case, both experimental and simulated HV indicate sub-surface straining up to $d/h \approx 10$. Simulated strain suggests up to a depth $d/h < 2$-4.

Fig. 18c shows an increased experimental surface hardness ($HV \approx 130$kg/mm^2), as in Figs. 18a,b but no hardness change for $d/h \geq 1$. If $\bar{\varepsilon} \approx 0.5$ at the depth h, as expected from simulations, and a Vickers indenter further increases the strain by 0.1-0.2 [58], HV at the depth h would be $\approx 15\%$ greater than that of the bulk, from the hardening curve of the CW009A as received copper (Fig. 6). That is not observed. In this case sub-surface straining may only be up to $d/h \leq 1$.
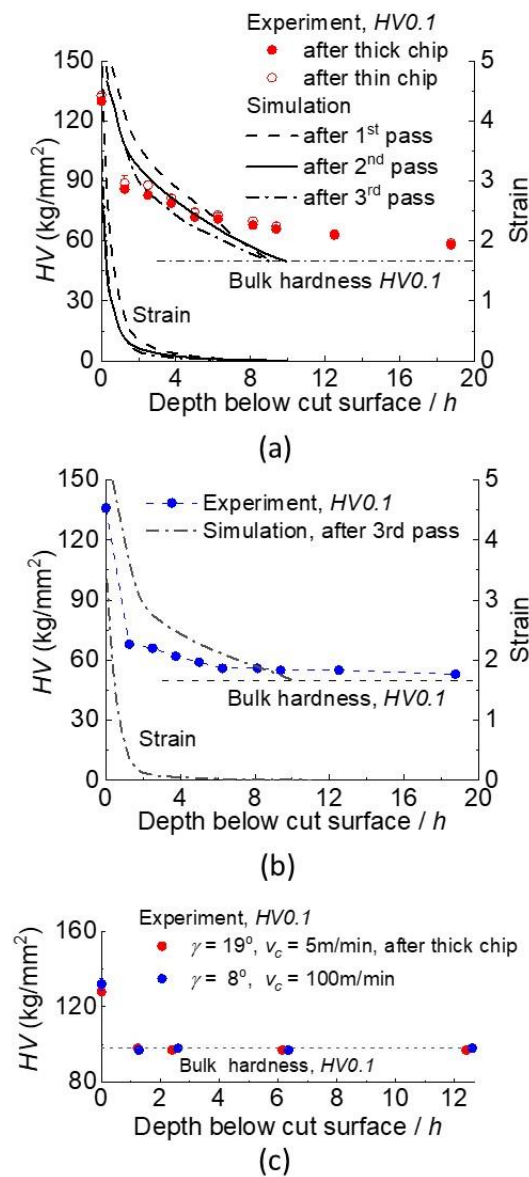
Fig. 18. Experimental hardness and simulated strain and hardness distributions below the cut surface. (a) CW008A as received $\gamma = 19°$, $v_c = 5$m/min. (b) CW008A as received $\gamma = 8°$, $v_c =$

100m/min. (c) CW009A as received $\gamma = 19°$, $v_c = 5$m/min and $\gamma = 8°$, $v_c = 100$m/min. (There are no simulations in part (c)). The red and blue colour codes continue the codings in Figs. 14 to 17.

Measurements other than of hardness show that cut surfaces after thin and thick cyclical chip formation differ from each other in two ways, within a depth up to $\approx 40\mu$m below the cut surface. Firstly Fig. 19a shows qualitatively that the surface texture after thin chip formation is finely grooved in the direction of cutting (presumably caused by roughness along the cutting edge) while, after thick chip formation, the grooving is partly disrupted by some form of damage. Secondly the etched sections of Figs. 20b,c show that the depth h_D over which the surface is dragged, as judged from displacement of grain boundaries, is substantially less after thin than thick chips.

Optical profilometry resolves the nature of the damage after thick chip formation and that it differs in scale between the CW008A (Fig. 20a) and CW009A (Fig. 20b) coppers. The underlying grooved surface from machining CW008A is interrupted by small pits up to $\approx 10\mu$m deep. In the case of CW009A the pits are larger and deeper, up to $\approx 20\mu$m. They appear as if caused by local shear failure and tearing of the surface as it passes under the cutting edge.

$h_D = 17 \pm 6\mu$m and $43 \pm 12\mu$m are obtained from the conditions of Figs. 19b,c. When measured values from the tests at both $\gamma = 19°$, $v_c = 5$m/min and $\gamma = 8°$, $v_c = 100$m/min, for both coppers, are taken together a correlation is found between h_D/h and t/h (Fig. 21). As t/h increases above ≈ 10, h_D/h increases above ≈ 0.5 and the surface damage seen in Fig. 20 occurs. Whether it is the value of h_D/h or the cyclical damage that drives the cyclical chip formation is discussed in Section 5.3.

The published literature reviewed in Section 1.2 reports deformed depth ratios d/h from < 1 to 20. This is the range observed here. It is seen to be strongly dependent on the assessment method.
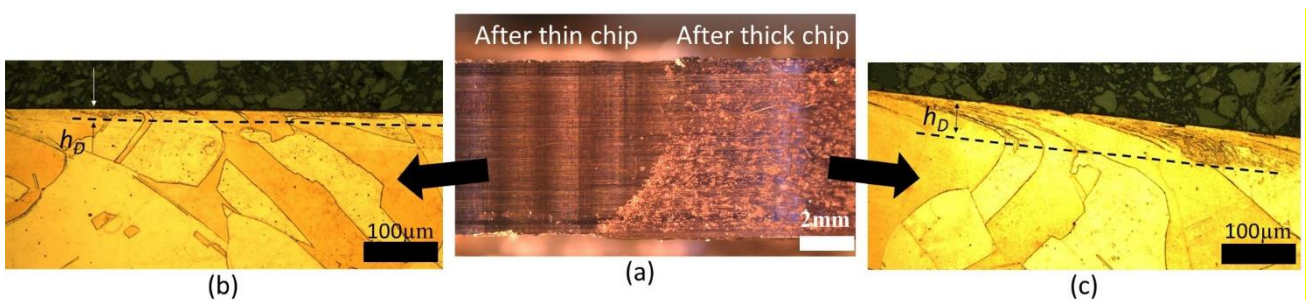

Figure 19. Cut surface plan and section views. (a) A plan macro view showing the changed surface when chip formation changes from thick to thin. (b) The cut surface section below a thin chip. (c) The cut surface section below a thick chip. The cut material is CW008A as received, $\gamma = 19°$ and $v_c = 5$m/min.
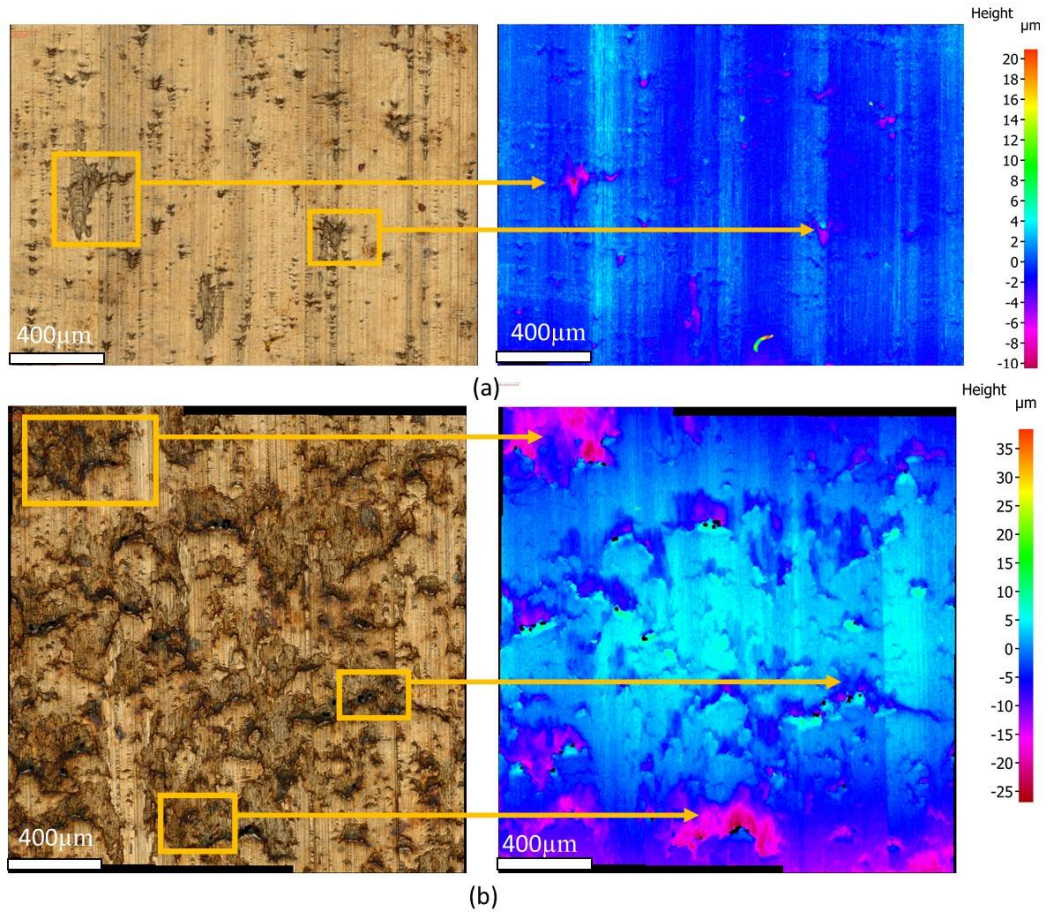
Fig. 20. Cut surface textures after thick chip formation. (a) Grooving and light damage in the case of as received CW008A. (b) Heavier damage in the case of as received CW009A. The cutting condition is v_c = 5m/min, γ = 19°.

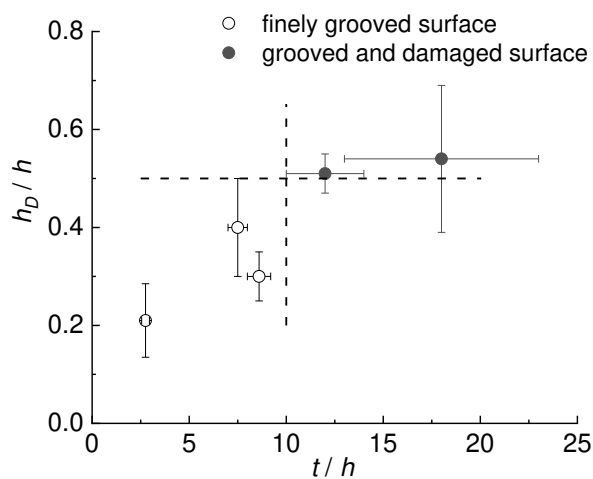**Fig. 21. Observed correlation between h_D/h and t/h.** As t/h increases, so does h_D/h and the surface texture changes from finely grooved to grooved with damage.

5. Discussion

5.1. *Results comparisons*

In the present work differences are seen between the simulated and experimental results when all three of $F_C{}^*$, $F_T{}^*$ and t/h are compared. It is useful to seek the sources of the differences through the derived dependencies of k on v_c and of $(\phi - \gamma)$ on λ, in the same way as it was useful in the Introduction to compare published results.

Fig. 22 gathers all the experimental and simulation results for k. k varies by ± 15% from its mean at any v_c. It is in accord with the scatter of values in Figs. 14 and 16. Experimentally k is in the range 250-350MPa when $v_c > 25$m/min, as with most previous work (Fig. 2b) but as v_c reduces below 25m/min, the experimentally derived k increase to 350-450MPa. This is not found in Fig. 2b though such high values can be deduced from [6,14]. The simulation results are near to a lower bound of the experimental results.

If k from the simulations were increased to agree with the experimental results, without change in t/h or the value of λ, simulated and experimental $F_C{}^*$ would be in agreement with the experimental values and the simulated $F_T{}^*$ would exceed them by 30-40% for both $\gamma = 8$ and 19°.
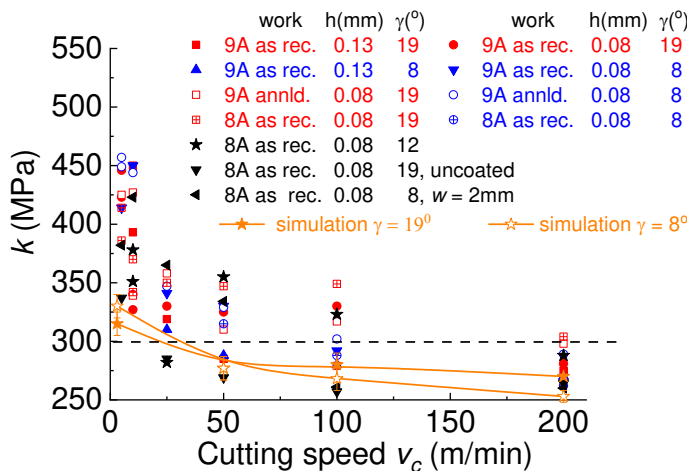

Fig.22. Experimental and simulated derived dependencies of k on v_c. The colour coding is carried forward from Figs. 14 to 17. The simulated results are near to lower bounds to the experimental results.

Fig. 23 compares dependencies of $(\phi - \gamma)$ on λ and also includes, as the + symbols, the results A-F from Fig. 2a. Results from cyclical chip formation conditions are represented by their averaged values. The cyclical condition is taken up in Section 5.3.

The main test $\gamma = 8$ and 19° results all lie within a band of width $\Delta\lambda \approx 3°$, with the $\gamma = 8°$ results grouped at higher $(\phi - \gamma)$ than the $\gamma = 19°$ results. The width $\Delta\lambda \approx 3°$ is approximately the size that

can be expected from tool use (Fig. 10). Within each group there is no significant difference between the results from the three different coppers.

The additional test results with the $\gamma = 12°$, AlCrN coated, and the 19°, uncoated, inserts are positioned at lower λ values than found in the main tests. It was speculated that uncoated tools would generate a higher friction coefficient sliding over copper. This is found not to be the case. The lower λ values for the $\gamma = 12°$ tests are part cause of the lower $F_C{}^*$, $F_T{}^*$ and t/h observed in Fig. 16, in addition to the direct influence of γ on these values.

The additional tests with $w = 2mm$ are positioned at higher values of λ. It was speculated that side spread of chips would reduce the friction resistance in the direction of sliding. Again, this is not the case.

The 3rd pass simulation results have the same character as the experimental results but are systematically displaced to higher values of λ, by 10-15°. If the simulated λ were reduced to the experimental values, without change in $F_C{}^*$, simulated and experimental $F_T{}^*$ would be brought into agreement.
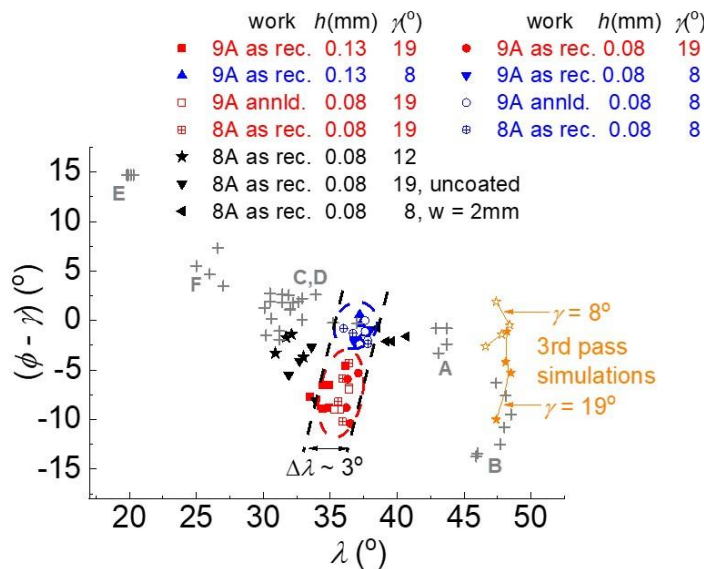

Fig. 23. Derived dependencies of $(\phi - \gamma)$ on λ. The figure includes the present experimental results (averaged values in cyclical conditions) and results from the 3rd pass simulations. Results from Figure 2a (A-F) are added as the + symbols. The present experimental results lie within a narrow range of λ. The simulation results are close to those from source B of previous work, though with larger values of $(\phi - \gamma)$.

From Figs. 23 and 24 it is concluded that there are two causes for the departure of the simulated from the experimental results. One is that particularly at low v_c there is insufficient strain hardening in the applied MTS plasticity model. The other is that at all v_c the friction stress (or the plastic flow stress at the chip / tool contact) is too large.

The last conclusion refers just to the present results. The 3rd pass simulation results are close to the experimental results B from Fig. 2a. Also the present experimental results with the AlCrN and uncoated inserts are close to the previous C, D results. None of the present results overlap the previous A, E or F results. Causes of λ variations in dry conditions are discussed in the next Section.

5.2. Modelling extensions

It is clear from the previous Section that the MTS model [41], which is well-validated in conditions that produce strains < 0.7, requires extension when larger strains occur. Here two physically-based but semi-empirical developments of the model improve agreement with experiments. One addresses under-estimating k at low v_c. The other addresses over-estimating friction.

Underestimating k is addressed by assuming a second obstacle to dislocation movement within grains, with a saturation stress $\beta\eta$ ($\beta > 1$). The evolution Eq. 6c is developed in a rule-of-mixtures way to Eq. 9a, with the second obstacle occupying a fraction α_{IV} of the total obstacle population. α_{IV} is taken to reduce with increasing temperature (Eq. 9b). Eq. 6c is regained when $\alpha_{IV} = 0$. A plausible value for β is 2 and a plausible range for α_{IV} at room temperature is 0.01 to 0.1 (L.M. Brown, Personal communication, 2020: see Acknowledgements). It is a convenient and physically justifiable way to include Stage IV hardening [51] in the model.

$$d\left(\sigma_t/\eta\right)\big/d\left(\bar{\varepsilon}/\eta\right)=\theta\left(\dot{\bar{\varepsilon}}\right)\left[\left(1-\alpha_{IV}\right)\left(1-\sigma_t/\eta\right)^2+\alpha_{IV}\left(1-\sigma_t/(\beta\eta)\right)^2\right] \qquad \sigma_t/\eta\leq 1$$

$$d\left(\sigma_t/\eta\right)\big/d\left(\bar{\varepsilon}/\eta\right)=\theta\left(\dot{\bar{\varepsilon}}\right)\alpha_{IV}\left(1-\sigma_t/(\beta\eta)\right)^2 \qquad \sigma_t/\eta > 1$$

(9a)

$$\alpha_{IV}=\alpha_{IV,20^o C}\left[\left(T_{\alpha,zero}-T\right)\big/\left(T_{\alpha,zero}-20\right)\right], \qquad T\leq T_{\alpha,zero}$$

$$\alpha_{IV}=0, \qquad\qquad\qquad\qquad\qquad T > T_{\alpha,zero}$$

(9b)

Reducing friction stress level is addressed by replacing Eq. 3a by Eq. 10. χ reduces from 1.0 to a lower value χ_{min} as strain increases from $\bar{\varepsilon}_{lower}$ to $\bar{\varepsilon}_{upper}$. It is a convenient though, as will be seen, oversimple way to introduce strain softening to the model.

$$\bar{\sigma}=\sigma_a+\chi s\left(\dot{\bar{\varepsilon}},T\right)\sigma_t$$

$$\chi=\frac{1+\chi_{min}}{2}+\frac{1-\chi_{min}}{2}\tanh\left[2\left(\frac{2\bar{\varepsilon}-\bar{\varepsilon}_{lower}-\bar{\varepsilon}_{upper}}{\bar{\varepsilon}_{lower}-\bar{\varepsilon}_{upper}}\right)\right]$$

(10)

Applying the extended modelling to simulations of compression testing at room temperature and low strain rate, creating the test geometry similarly to the way in which tensile test geometries are created (Appendix A3), and extracting stress / strain elemental data as compression progresses, leads to the strain hardening curves Figs. 24a,b. Fig. 24a shows the influence of α_{IV} with $\beta = 2.0$, in the absence of strain softening ($\chi_{min} = 1.0$). Fig. 24b shows the influence of χ_{min} when $\alpha_{IV} = 0.08$, $\bar{\varepsilon}_{lower}$ = 3 and $\bar{\varepsilon}_{upper}$ = 8.

Fig. 24c shows flow stress contours from a chip formation simulation taking $\alpha_{IV,20°C} = 0.08$ and $T_{\alpha,zero} = 250°C$, and $\chi_{min} = 0.5$ (with $\beta = 2.0$, $\bar{\varepsilon}_{lower}$ = 3 and $\bar{\varepsilon}_{upper}$ = 8). These values are chosen as extreme feasible values, illustrative of the sensitivity of chip formation predictions to the proposed MTS model extensions. The slope of the strain hardening curve (Fig. 24a) when $\alpha_{IV} = 0.08$ is $\approx$ 21MPa over the strain range 3-8, approximately half of values measured over the strain range 1-3 [59]. The strain softening range of 3 to 8 is taken from [30] with $\chi_{min} = 0.5$ less than the value ≈ 0.53 from data in that paper. A reduced flow stress is predicted in the chip in contact with the tool, leading to a reduced friction. The following simulations here are with these additional coefficient values.

(Alternatively, and more natural to the model, softening could be introduced as σ_t/η increases. Softening as σ_t/η increases from 1.05 to 1.25 would replace softening as strain increases from 3 to 8.)
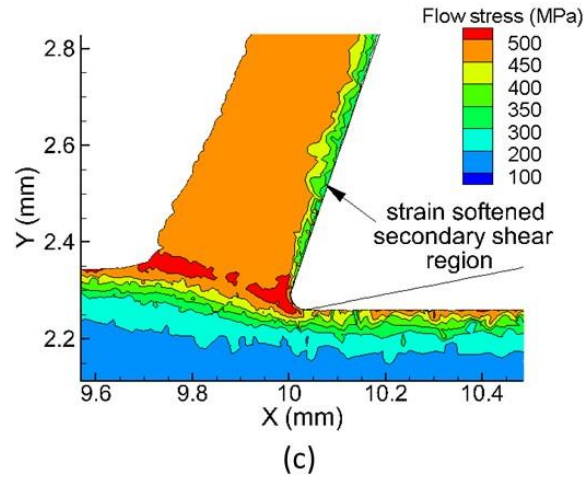

(a)

(b)

(c)
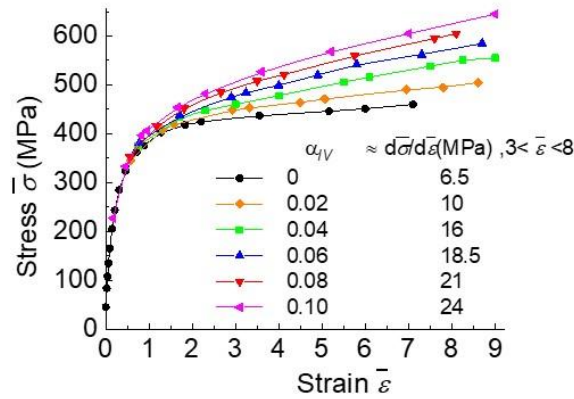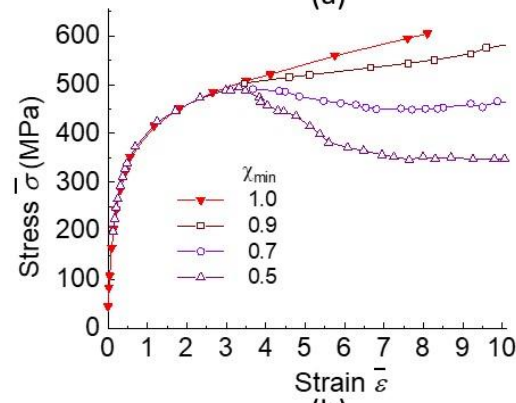
Fig. 24. MTS model developments. (a) The influence of stage IV hardening coefficient α_{IV} on strain hardening at $T = 20°C$ and $\dot{\bar{\varepsilon}} = 10^{-3}$/s, in the absence of strain softening. (b) The influence of strain softening parameter χ_{min} when $\alpha_{IV} = 0.08$. (c) An example chip formation showing reduced flow stress in the chip in contact with the tool when $\alpha_{IV,20°C} = 0.08$, $T_{\alpha,zero} = 250°C$ and $\chi_{min} = 0.5$. The example is for a 3rd pass simulation with $\gamma = 19°$, $h = 0.08$mm and $v_c = 25$m/min. The colour coding in (a) and (b) is to guide the eye,

Fig. 25 shows a better agreement than does Fig. 22 between simulated and experimental dependence of k on v_c particularly for $v_c \geq 25$m/min. The differences between simulated and experimental values at $v_c = 5$m/min still exist but are much reduced. Fig. 26 shows the simulated values of λ to be reduced by strain softening to the range found experimentally. The main purpose of the modelling, to determine the rake face friction from the copper's flow stress rather than from an assumed friction coefficient, is achieved.
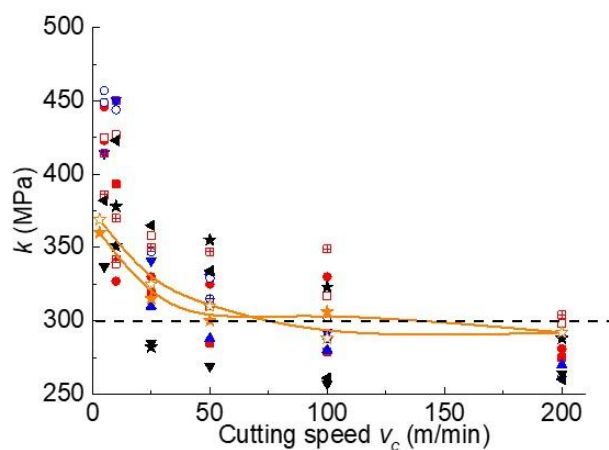

Fig. 25. **Experimental and modified simulated derived dependencies of k on v_c.** The modified simulations are in better agreement with experiment than is seen in Fig. 22. The symbols and colour coding are the same as in Fig. 22.
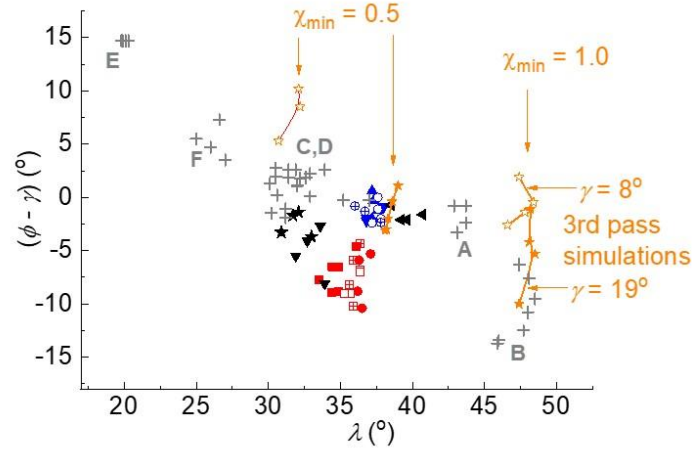
Fig.26. **Derived dependencies of ($\phi - \gamma$) on λ**. The figure repeats Fig. 23 but with some annotations removed for clarity and with both original and extended simulation results. The extended simulations produce lower λ values than those from the original simulations. The symbols and colour coding are the same as in Fig. 23.

However two problems remain. One is that the simulated λ values in Fig. 26 are lower for the $\gamma = 8°$ than the 19° inserts whereas experimentally λ in the main test series is independent of γ, as also is the simulated λ in the absence of strain softening. To relate χ to a constant strain range and possibly to consider it only acting to reduce σ_t (Eq. 10) is oversimple. It is an open question whether some further empirical but simple extension of Eq. 10 could adequately improve the simulations or whether a move is necessary to a more complex dynamic recrystallization modelling of strain softening, as in [43, 44]. The other is that the simulated ϕ values, also in Fig. 26, become too large (t/h becomes too small). F_C*, F_T* as well as t/h are all systematically underestimated by the 3rd pass simulations. It is not currently clear how much this is due to limitations of the MTS modelling extensions or of the simulations' ability accurately to capture the strains in the cut surface that in part control the 3rd pass chip formation (Figs. 19a,b show differences between the measured and simulated hardness profiles beneath the cut surfaces), or whether it stems from the friction law which focuses on the plastic fraction of the chip / tool contact at the expense of the elastic fraction.

It is asked in Section 1.2 whether thermal softening of the chip bulk occurs only after chip formation and whether strain softening at the chip / tool contact occurs during chip formation. The answer to both, from the results here, is yes. Strain softening is known to be sensitive to purity of the copper [28, 29]. It can explain some of the historically observed wide range of λ. The present materials are all $\geq$ 99.99% Cu and the simulation results span $\lambda = 31\text{-}39°$. The material B (Fig. 26) is 97.8% Cu: its value of λ is as if there is no strain softening. The purity of material A is not known but a single simulation (not presented) with $\gamma = 19°$, $\chi_{min} = 0.7$ gives $\lambda = 43°$. To explain $\lambda < \approx 31°$

requires some other factor. At higher cutting speeds it could be additional thermal softening. That can explain the historical data E. The present results with uncoated and AlCrN coated tools demonstrate that the tool surface material influences friction but this is not accommodated in the friction model Eq. 4. The present simulations apply $\mu_f = 2.0$ to activate plastic flow over the chip / tool contact but a split tool test has observed plastic flow in the contact next to the cutting edge with Coulomb friction and $\mu_f = 1.0$ in the elastic region at the tail of the contact [30]. It is plausible that the λ values of the historic data A-F but excluding E arise from a combination of varying strain softening and with μ_f in the range 1.0 to 2.0. The present software's friction implementation is not sensitive enough to check this.

5.3. *Cyclical chip formation and the cut surface state*

It is asked in the Introduction why cyclical chip formation, in the absence of surface active coatings, has only rarely been reported in studies of copper machining (in references [12,13] in contrast to [1-9]). The present experimental work finds cyclical chip formation for all three copper materials, at all rake angles studied, clearly for $v_c = 5$ and 10m/min and up to 50m/min when $w = 2$mm ($w = 6$mm gives rise to a less clear transition condition as v_c increases from 25 to 50m/min). The simulations do not predict this.

An answer from the experiments is that $t/h \approx 10$ is a critical value for cyclical formation. Only in [4], [12,13] and in the present experiments is this value exceeded. That the simulations do not predict this may arise from the observed cyclical state being more complex than previously recognized. With the CW009A copper, both as received and annealed, the chip formed during the thick phase of the cycle (Fig. 11b) has t/h capped at ≈ 10-15. With CW008A t/h can reach double this value (Fig. 11d). Cyclical chip formation occurs with CW009A as received despite it being in a pre-strained state (Fig. 6), although it is recognized that its Vickers hardness of ≈ 100kg/mm^2 is still substantially less than the chip hardness of 140kg/mm^2.

The previous works [12, 13] propose a cyclical state of strain hardening beneath the cut surface as driving the cyclical behaviour. Fig. 18 shows no significant difference between sub-surface strain hardening after thick or thin chip formation with CW008A (Fig. 18a), and a very different hardness distribution in the case of CW009A as received (Fig. 18c). A conclusion is that, in the present work, it is not cyclical hardening beneath the cut surface that drives the cyclical behaviour, at least over the depth scale $d = 10$-20h (Fig. 18a).

The present work does show cut surface differences after thick and thin cyclical chip formation on a scale $d < 0.5h$ (this depth range, $d < 40\mu$m, is not accessible to the present work's hardness testing at 0.1kg load because of the requirement that there be a minimum distance between an indentation

and the specimen edge). The thick chip with $t/h > 10$ leaves a cut surface which is damaged (Fig. 20) and beneath which there is a dragged layer h_D to a depth $\approx 0.5h$ (Fig. 21). At the next pass of the tool the chip is thinner, the surface damage does not occur and h_D becomes $\approx 0.2h$.

It is possible that it is the near-surface hardness ($d < 0.5h$) that determines the cyclical behaviour. The simulations (Fig. 18a) show 1st pass chip formation to cause $\bar{\varepsilon} > 2$ up to a depth $d \approx 0.5h$, with $HV \approx 150\text{kg/mm}^2$ estimated, and that this results in a thin chip at the 2nd pass, with a similarly hardened depth only to $d \approx 0.2h$. However, the hardening at the 2nd pass is sufficient to prevent the regaining of the thick chip formation at the 3rd pass. An alternative but tentative proposal is that it is the surface damage that drives the cycling. Its different severity between CW008A and CW009A copper (Fig. 20) may be placed alongside the different severities taken by the thick chips from these two (Figs. 11b,d) while $h_D \approx 40\mu\text{m}$ for both. It would in part explain the simulations' failures to predict the cycling. The plasticity model has no damage and failure criterion. However this proposal would require the damaged free surface to modify chip formation, to reduce deformation in the cut surface at the 2nd pass relative to that without damage, to recover thick chip formation at the 3rd pass. We have no mechanism for this. We compare the present observations with cyclical chip formation when a copper surface is coated at regular intervals by an active medium. It is suggested in that case that the active medium changes flow by embrittling the surface [15, 16] though the mechanism of embrittlement remains an open question [16] and what would happen at the 2nd pass over a previously partly coated surface has not been reported. In the present work k and λ during the thick chip and λ during the thin chip phase of cyclical formation are close to those reported in [15] though k in the thin chip phase is not reduced. In [13] the thin chip phase during machining 70/30 brass in the absence of surface coating is described as a brittle flow, though k (calculated from given F_C, F_T and t/h to be 270MPa) is greater than in the thick chip phase ($k = 240$MPa). Further study is required.

A practical lesson is that $v_c > 100$m/min avoids the uncertainties of cyclical formation.

6. Conclusion

Experimental results are reported of all of cutting and thrust forces and chip thickness ratio, as well as of chip and cut surface hardness, from orthogonal machining of OFHC copper in general engineering conditions (cutting speeds v_c from 5-200m/min, rake angles 8 to 19° and uncut chip thickness ≈ 0.1mm). Cut surface texture is also imaged. The coppers are of two grades, both Cu > 99.99%, one in an as received drawn condition as well as after annealing and the other in an as received hot extruded state. The purpose has been to provide this breadth of data within a single source rather than spread across many sources as is mostly the case in the published literature.

The cutting and chip thickness results are analysed in classical terms of forces resolved on to the nominal shear plane area. The shear stress k so obtained is a measure of the resistance of the copper to chip formation. The relation between the shear plane angle ϕ and the sliding friction angle λ between chip and tool is also obtained (the shear plane angle is a proxy for the chip thickness ratio). The classical analysis provides a way of later comparing the experimental with simulation results, together with enabling insights into reasons for differences between them. It is found to be useful, contrary to views in a number of recent papers that claim such an approach is inappropriate.

For $v_c \geq 25$m/min k is calculated to be in the range 250-350MPa, in agreement with most previous studies. As v_c reduces below 25m/min k increases to the range 350-450MPa. It is a more narrow range than the 300-500MPa found from previous work. Over all the experiments the friction angles λ are determined in the range 30-40°, with most values from 32-37°. It is a much more narrow range than values from the literature of from 20° to 48°.

The experimental results provide validation for finite element simulations in which the copper plasticity is described by a Mechanical Threshold Stress model. A friction coefficient is not required as input. Instead the friction stress between chip and tool is obtained naturally from the plasticity model in the deformation conditions at the chip / tool contact. In a main set of simulations the model includes only stage III strain hardening and does not include strain softening. Coefficients of the model are well-established from the literature. Shear stresses k obtained from resolving forces on to the shear plane, as with the experimental results, slightly underestimate the experimental values. In particular they do not predict the large increase in k for $v_c < 25$m/min. Further, the obtained values of λ exceed the experimental values by 10-15°.

In a preliminary set of additional simulations both stage IV hardening and strain softening are introduced empirically. The increased strain hardening brings the simulated and experimental values of k into agreement. Strain softening reduces the simulated λ to the experimental range but at the present time simulated values of ϕ are too high. Although this discrepancy remains, it is demonstrated that a pre-determined friction coefficient is not required as an input to the simulations.

It is speculated that the wider range of λ found in the literature than in the present work comes at least in part from variability of strain softening characteristics between coppers of different purity (the experiments and simulations suggest that strain softening adjacent to the rake face occurs during the chip formation but thermal annealing found in chips after machining occurs after the chip formation).

An experimental observation at the lowest cutting speeds, occasionally reported in previous literature, is cycling of chip thickness and forces from high to low values from one pass of the tool over the work to the next. It occurs with all work material and tool rake angle combinations studied

here. Cut surface damage as well as sub-surface hardening is found after the thick chip phase of the cycle. It is proposed that damage is important for the cycling behaviour but what is the mechanism is an open question.

It was asked at the start of this paper what are the fundamental problems in applying physical modelling to predictions of chip formation during machining highly ductile metals such as annealed copper. The answer certainly includes extending constitutive models to strains in the range 5 to 10.

Appendix A. Model further details

A.1. *Simplification in constant strain rate and temperature conditions*

θ and η remain constant during a flow at constant strain rate and temperature. Eq. 2c, with Eq. 6c, can be re-written as Eq. A1 in a flow with the initial state $(\sigma_t/\eta)_{initial} \neq 0$ and the initial strain $\bar{\varepsilon}_{initial} = 0$. It is a standard integral. Eq. A2 is obtained. The MTS model strain hardening curve in Fig. 6 is obtained from this with $(\sigma_t/\eta)_{initial} = 0.1$.

$$\int_{\sigma_{t,initial}}^{\sigma_t} \frac{d\sigma_t}{\left(1-\sigma_t/\eta\right)^2} = \theta \int_0^{\bar{\varepsilon}} d\bar{\varepsilon} \tag{A1}$$

$$\sigma_t = \eta \left\{ 1 - \frac{1}{1 \Big/ \left[1 - \left(\frac{\sigma_t}{\eta}\right)_{initial} \right] + \left(\frac{\theta}{\eta}\right)\bar{\varepsilon}} \right\} \tag{A2}$$

A.2. *Model implementation*

Fig. A1 presents an overview of the implementation of Eq. 7. At each time step, temperature, strain rate and time step duration are input to the user-defined subroutine from the main program, with the previous time step's values of strain, saturation stress and σ_t/η from local memory. Strain, saturation stress and σ_t/η are updated and returned to local memory; and $\bar{\sigma}_n$ is calculated and returned to the main program, by means of the six steps listed in the figure.
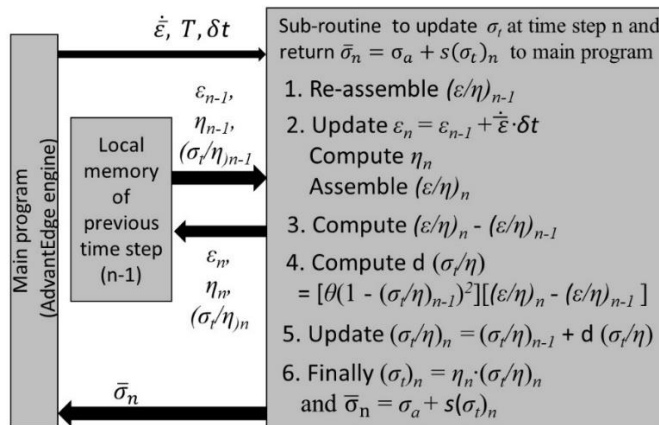

Fig. A1. An outline of the computation scheme.

One modification is found to be necessary. $\dot{\bar\varepsilon}$ as a variable in the expression for η (Eq. 6b) is replaced by a constant representative strain rate v_c/h, but not in the expressions for s (Eqs. 5a,b). Otherwise the simulation becomes unstable. v_c/h is close to the maximum strain rate in the primary shear region.

A further modification compensates for simulations at v_c = 5m/min being expected to take an excessively long time: $\approx$ 1 month is estimated. The results presented in Section 4 for v_c = 5m/min are in fact isothermal calculations, run at v_c = 100m/min. Temperature in Eqs. 5b, 6b is set at 293K and $\dot{\bar\varepsilon}$ is changed to $0.05\,\dot{\bar\varepsilon}$, to regain flow stress values relevant to 5m/min. For the record, an approximate simulation actually at v_c = 5m/min and allowing temperature to vary gives a chip temperature rise of 25°C.

A.3. *Tensile test validation of the computation scheme*

It is possible to create a tensile test geometry using the software's machining geometry pre-processor. Fig. A2a shows a geometry created for the tool ($v_x = v_y = 0$) and work (v_x = 300m/min, v_y = 0). x-displacement of the work causes two struts to stretch. Fig. A2b shows strain and necking in the struts after a relative displacement of $\approx$ 3mm, in this example when the strut gauge length $\approx$ 5mm.

The velocity of 300m/min, with the gauge length 5mm, generates a strain rate $\approx 10^3$/s in the struts. Strain rates of 10^4 and 10^5/s are generated by reducing the work and tool size 10-fold and 100-fold while keeping v_c = 300m/min. A strain rate equivalent to 10^{-3}/s is generated by reducing v_x to 3m/min and also by de-rating the plasticity model's strain rate sensitivity by a factor 10^4 and removing its temperature dependence.

Examples of strain, temperature and strain rate in a strut shortly before necking starts are in Fig. A3. There is a uniformity of strain and temperature over the gauge length. Strain rate is more variable.
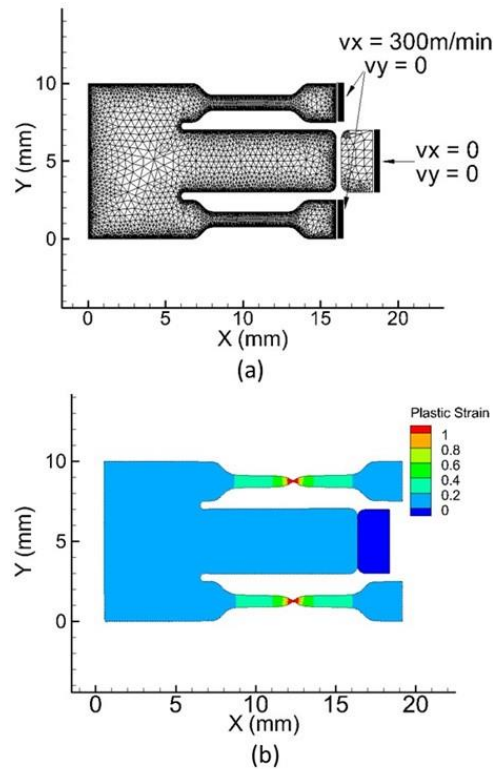
Fig. A2. A tensile test simulation. (a) The test geometry and boundary conditions. (b) An instant from the test showing necking. (a) generates a strain rate ≈ 10^3/s. Other strain rates are generated by changing the scale of the model.
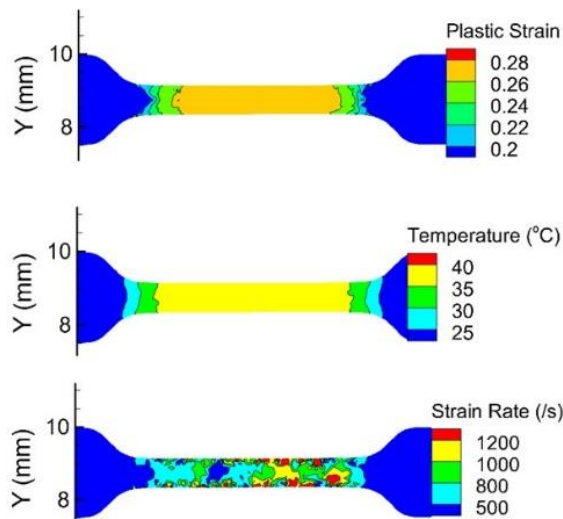

Fig. A3. Example strain, temperature and strain rate contours before necking. The work size and velocity boundary condition are as in Fig. A1.

The time stepping implementation, Eq. 7 (Fig. A1), with the tensile test geometry and MTS model inputs (Tables 3 and 4), is applied to obtain load - extension curves. Load W is converted to engineering stress W/A_0, with A_0 the original cross-section. Engineering stress – extension curves are also obtained by direct calculation from Eq. 3a, with s from Eq. 5b and σ_t from Eq. A2 and, for the purpose of comparison, taking into account that the simulations are in plane strain. Fig. A4 compares

51

the two. The simulations successfully follow expectations from direct calculation, with differences between the two < 5%.
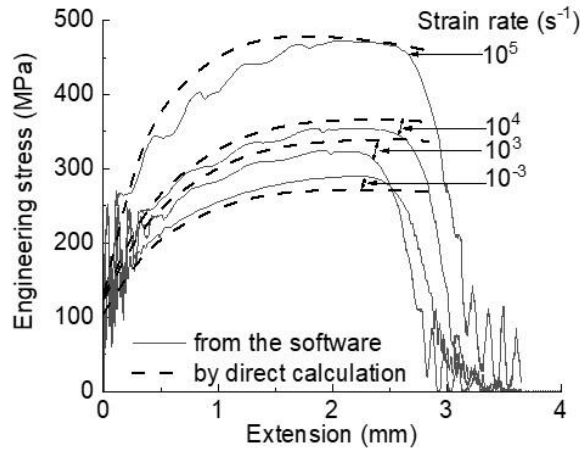

Fig. A4. Tensile test engineering stress v. extension curves. The solid lines from simulations are in satisfactory agreement with the dashed lines from direct calculation. Extensions are re-scaled to a common base (gauge length 5mm).

Appendix B. Software meshing detail

B.1. *Ploughing force determination and influence on cutting forces*

Fig. B1 is a detail of the tool cutting edge region. In this example ($\gamma = 8°$, $r_\beta = 20\mu m$) the nodes labelled 1 to 15 are on the edge radius. The x- and y-component reactions of the work on the tool through these nodes can be extracted and their resultant directions calculated, to determine the position of the neutral point. Between the neutral point and node 1 the direction of the resultant force indicates flow of work material into the chip; from the neutral point to node 15 flow is into the cut surface. It is the sum of the nodal forces from the neutral point to node 15 that is considered to be the ploughing force. The x-sum gives the ploughing cutting force $F_{C,P}$ and the y-sum gives the ploughing thrust force $F_{T,P}$.

$F_{C,P}$ and $F_{T,P}$ can be non-dimensionalised with respect to the edge radius r_β and the calculated shear stress k on the shear plane. The simulations in this paper give $F_{C,P}/(kr_\beta)$ and $F_{T,P}/(kr_\beta)$ in the range 0.75 to 2. This is similar to the range found in previous studies of steel machining [60]. These values are sufficiently small that they do not significantly influence conclusions from this work. Examples are in Appendix B2.
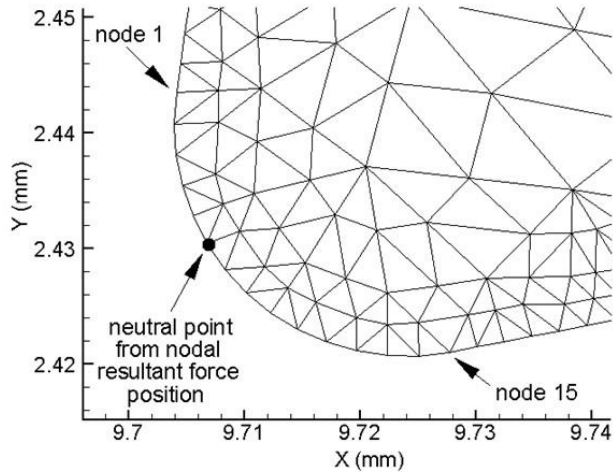
Fig. B1. Tool meshing round the cutting edge. Nodes 1 to 15 define the tool nose radius, with the neutral point indicated between them.

B.2. *Work meshing control*

A user has partial control of the workpiece meshing. In addition to choosing the minimum mesh size in a continuous manner, the aggressiveness of mesh refinement under increasing plastic severity and of mesh coarsening under reducing severity are separately controllable in a step-wise manner. In the present work, in addition to selecting minimum mesh size between ¼ and ½ of r_β, it is found necessary to select mesh refinement from 1 to 2 steps finer and coarsening from 2 to 3 steps finer than the default settings.

The computation time per cut distance increases with cut distance, as the number of nodes in the refined cut surface increases (Fig. 7a). It also increases with reduction of minimum mesh size and fineness of refinement/coarsening. These also cause the total number of nodes to increase. Counter-intuitively, re-meshing problems, leading to computation failure, increase at the chip free-surface as mesh size reduces.

With $\gamma = 8°$ and $v_c \le 50$m/min, the cut distance to achieve a steady state exceeds 12mm. With $r_\beta = 20$μm, minimum mesh size is 5 to 10μm and computation times exceed 12 days, with a significant possibility of computation failure. For these reasons, in these γ and v_c conditions, $r_\beta = 30$μm is chosen in this work, allowing minimum mesh size to be increased to 15μm. Then the predicted F_C and F_T are adjusted to the values expected for $r_\beta = 20$μm, by correcting for too large a ploughing force in the manner indicated in Appendix B1. F_C and F_T are reduced by 3N/mm and 5N/mm respectively for $v_c = 50$ and 5m/min.

The additional simulations in Section 5 are also carried out with $r_\beta = 30$μm, with reductions of 4N/mm in F_C and F_T needed to correct them to $r_\beta = 20$μm values. With $r_\beta = 30$μm, elapsed

computing times are in the range 3-6days. Fewer meshing and convergence computational failures occur.

REFERENCES

[1] A.J. Chisholm, A review of some basic research on the machining of metals, In: Proc. I. Mech E. Conf. on Technology of Engineering Manufacture, London (1958) pp.227-236.

[2] H.Ll.D. Pugh, Mechanics of the cutting process, In: Proc. I. Mech E. Conf. on Technology of Engineering Manufacture, London (1958) pp.237-254.

[3] N.N. Zorev, Metal Cutting Mechanics, Pergamon Press, Oxford (1966), Figures 213, 214.

[4] J.E. Williams, E.F. Smart, D.R. Milner, The metallurgy of machining Part 1: basic considerations and the cutting of pure metals; Part 2: The cutting of single phase, two-phase and some free machining alloys, Metallurgia, 81 (1970), pp.3-10 and 51-59.

[5] P.K. Wright, J.L. Robinson, Material behaviour in deformation zones of machining operation, Metals Technology, 4 (1977), pp.240-248. https://doi.org/10.1179/030716977803292042.

[6] K.J. Trigger, B.F. von Turkovich, Chip formation in high-speed cutting of copper and aluminium, Trans ASME J. Eng. Ind., 85 (1963), pp. 365-372. https://doi.org/10.1115/1.3669895.

[7] B.F. von Turkovich, K.J. Trigger, Theoretical aspects of high-speed-shear in face centered cubic metals, Trans ASME J. Eng. Ind., 85 (1963), pp. 357-363. https://doi.org/10.1115/1.3669892.

[8] P. Fernandez-Zelaia, S.N. Melkote, Process-structure-property relationships in bimodal machined microstructures using robust structure descriptors, J. Mater. Process. Technol., 273 (2019), 116251. https://doi.org/10.1016/j.jmatprotec.2019.116251.

[9] P. Fernandez-Zelaia, S.N. Melkote, Analysis of structure-property gradients in orthogonally machined chips and workpiece subsurface, CIRP Ann. Manuf. Technol., 69 (2020), pp. 89-92. https://doi.org/10.1016/j.cirp.2020.04.020.

[10] M.E. Merchant, Mechanics of the metal cutting process. II plasticity conditions in orthogonal cutting, J. Appl. Phys., 16 (1945), pp.318-324. https://doi.org/10.1063/1.1707596.

[11] E.H. Lee, B.W. Shaffer, The theory of plasticity applied to a problem of machining,

Trans ASME Jnl. Appl. Mech., 18 (1951), pp.405-413.

[12] H. Yeung, K. Viswanathan, A. Udupa, A. Mahato, S. Chandrasekar, Sinuous flow in cutting of metals, Phys. Rev. Appl., 8 (2017), 054044. https:doi.org/10.1103/PhysRevApplied.8.054044.

[13] K. Nakayama, The formation of saw-toothed chip in metal cutting, In: Proceedings of the 1st Int .Conf. on Production Engineering. Tokyo, Japan: Japan Society of Precision Engineering (1974) vol. 1, pp. 572–577.

[14] A. Udupa, K. Viswanathan, H. Yeung, S. Chandrasekar, The cutting of metals via plastic buckling, Proc. R. Soc., A473 (2017), 20160863. https://doi.org/10.1098/rspa.2016.0863.

[15] A. Udupa, T. Sugihara, J.B. Mann, Glues make gummy metals easy to cut, J. Manuf. Sci.Eng., 141 (2019), 091011. https://doi.org/10.1115/1.40444158.

[16] A. Udupa, A.S. Vandana, M. Saei, D. Gupta, J.B. Mann, K. Viswanathan,, N.K. Sundaram, Sinuous plastic flow: mechanics, microstructural basis, and control, Int. J. Mach. Tools Manuf., 168 (2021), 103728. https://doi.org/10.1016/j.ijmachtools.2021.103728.

[17] H. Yeung, K. Viswanathan, W.D. Compton, S. Chandrasekar, Sinuous flow in metals, Proc. Natl Acad. Sci. USA, 112 (2015), 9828–9832. https://doi.org:10.1073/pnas.1509165112.

[18] D. Sagapuram, A. Udupa, K. Viswanathan, J.B. Mann, R. M'Saoubi, T. Sugihara, S. Chandrasekar, On the cutting of metals: a mechanics viewpoint, J. Manuf. Sci. Eng., 142 (2020), 110808. https://doi.org/10.1115/1.4047869.

[19] T.L. Brown, C.L. Saldana, T.G. Murthy, J.B. Mann, Y. Guo, L.F. Allard, A.H.King, W.D. Compton, K.P. Trumble, S. Chandrasekar, A study of the interactive effects of strain, strain rate and temperature in severe plastic deformation of copper, Acta Materialia, 57 (2009), pp.5491-5500. https://doi.org/10.1016/j.actamat.2009.07.052.

[20] S. Shekhar, J. Cai, J. Wang, M.R. Shankar, Multimodal ultrafine grain size distributions from severe plastic deformation at high strain rates, Mat. Sci. Eng. A, 527 (2009), pp. 187-191. https://doi.org/10.1016/j.msea.2009.07.058.

[21] S. Abolghasam, S. Basu, S. Shekhar, J. Cai, M.R. Shankar, Mapping subgrain sizes resulting from severe simple shear deformation, Acta Materialia 60 (2012), pp. 376-386. https://doi.org/10.1016/j.actamat.2011.09.055.

[22] S. Shekhar, S. Abolghasem, S. Basu, J. Cai, M.R. Shankar, Effect of severe plastic deformation in machining elucidated via rate-strain-microstructure mappings, J. Manuf. Sci. Eng., 134 (2012). 031008, https://doi.org/10.1115/1.4006549.

[23] M. Elmadagli, A.T. Alpas, Metallographic analysis of the deformation microstructure of copper subjected to orthogonal cutting, Mater. Sci. Eng., A355 (2003), pp.249-259. https://doi.org/10.1016/S0921-5093(03)00072-8.

[24] H. Ni, A.T. Alpas, Sub-micrometer structures generated during dry machining of copper, Mater. Sci. Eng., A361 (2003), pp.338-349. https://doi.org/10.1016/S0921-5093(03)00530-6.

[25] A. Raczy, M. Elmadagli, W.J. Altenhof, A.T. Alpas, An Eulerian finite-element model for determination of deformation states of a copper subjected to orthogonal cutting, Metall. Mater. Trans A35 (2004), pp. 2393-2400. https://doi.org/10.1007/s11661-006-0219-3.

[26] J. Zhang, X. Xu, J. Outeiro, H. Liu, W. Zhao, Simulation of grain refinement induced by high-speed machining of OFHC copper using cellular automata method, J. Manuf. Sci. Eng., 142 (2020). 091006, https://doi.org/10.1115/1.4047431.

[27] H. Liu, J. Zhang, B. Xu, X. Xu, W. Zhao, Prediction of microstructure gradient distribution in machined surface induced by high speed machining through a coupled FE and CA approach, Mater. Des., 196 (2020) 109133. https://doi.org/10.1016/j.matdes.2020.109133.

[28] A.I. Almazrouee, K.J. Al-Fadhalah, S.N. Alhajeri, T.G. Langdon, Microstructure and microhardness of OFHC copper processed by high-pressure torsion, Mat. Sci. Eng. A, 641 (2015), pp. 21-28. https://doi.org/10.1016/j.msea.2015.06.016.

[29] X.H. An, S.D. Wu, Z.F. Zhang, R.B. Figueiredo, N. Gao, T.G. Langdon, Evolution of microstructural homogeneity in copper processed by high-pressure torsion, Scripta Materialia 63 (2010), pp. 560-563. https://doi.org/10.1016/j.scriptamat.2010.05.030.

[30] S. Kato, K. Yamaguchi, M. Yamada, Stress distribution at the interface between tool and chip in machining, J. Manuf. Sci. Eng., 94 (1972), pp. 683-689. https://doi.org/10.1115/1.3428229.

[31] D. Haslam, C. Rubenstein, Surface and sub-surface work-hardening produced by the planing operation, CIRP Ann. – Manuf. Technol., 18 (1970), pp.369-381.

[32] J.C. Outeiro, S. Campocasso, L.A. Denguir, G. Fromentin, V. Vignal, G. Poulachon, Experimental and numerical assessment of subsurface plastic deformation induced by OFHC copper machining, CIRP Ann. – Manuf. Technol., 64 (2015), pp. 53-56. https://doi.org/10.1016/j.cirp.2015.04.080.

[33] R. Calistes, S. Swaminathan, T.G. Murthy, C. Huang, C. Saldana, M.R. Shankar, S. Chandrasekar, Controlling gradation of surface strains and nanostructuring by large-strain machining, Scripta Materialia 60 (2009), pp.17-20. https://doi:10.1016/j.scriptamat.2008.08.027.

[34] Y. Guo, R. M'Saoubi, S. Chandrasekar, Control of deformation levels of machined surfaces, CIRP Ann. – Manuf. Technol., 60 (2011), pp. 137-140. https://doi.org/10.1016/j.cirp.2011.03.138.

[35] J.A. Bailey, S. Jeelani, Determination of subsurface plastic strain in machining using an embossed grid, Wear 36 (1979), pp.199-206. https://doi.org/10.1016/0043-1648(76)90005-3.

[36] G.R. Johnson, W.H. Cook, A constitutive model and data for metals subjected to large strains, high strain rates, and high temperatures, In: Proceedings of the 7th Intnl. Symp. on Ballistics. The Hague, Netherlands (1983) pp. 541-547.

[37] H. Ding, N. Shen, Y.C. Shin, Modeling of grain refinement in aluminium and copper subjected to cutting, Comput. Mater. Sci., 50 (2011), pp. 3016-3025. https://doi.org/10.1016/j.commatsci.2011.05.020.

[38] A.S. Vandana, N.K. Sundaram, Simulation of sinuous flow in metal cutting, Tribol. Lett., 66 (2018), 94. https://doi.org/10.1007/s11249-018-1047-5.

[39] A.S. Vandana, N.K. Sundaram, Simulation of machining of ductile polycrystalline aggregates using a remeshing framework, J. Manuf. Process., 54 (2020), pp.1-13. https://doi.org/10.1016/j.jmapro.2020.02.041.

[40] L.A. Denguir, J.C. Outeiro, G. Fromentin, V. Vignal, R. Besnard, Orthogonal cutting simulation of OFHC copper using a new constitutive model considering the state of stress and microstructure effects, Procedia CIRP, 46 (2016), pp. 238-241. https://doi.org/10.1016/j.procir.2016.03.208.

[41] P.S. Follansbee, U.F. Kocks, A constitutive description of the deformation of copper based on the use of the mechanical threshold stress as an internal state variable, Acta Metallurgica, 36 (1988), pp.81-93. https://doi.org/10.1016/0001-6160(88)90030-2.

[42] Z. Atmani, B. Haddag, M. Nouari, M. Zenasni, Combined microstructure-based flow stress and grain size evolution models for multi-physics modelling of metal machining, Int. J. Mech. Sci., 118 (2016), pp.77-90. https://doi.org/10.1016/j.ijmecsci.2016.09.016.

[43] R. Liu, M. Salahshoor, S.N. Melkote, J. Subramaniam, T. Marusich, A unified approach to modeling material behavior and microstructure evolution in machining of OFHC Copper, In: Proceedings of the ASME 2014 International Manufacturing Science and Engineering Conference, MSEC2014-4180, V001T01A011. https://doi.org/10.1115/msec2014-4180.

[44] R. Liu, M. Salahshoor, S.N. Melkote, T.D. Marusich, A unified material model including dislocation drag and its application to simulation of orthogonal cutting of OFHC Copper, J. Mater. Process. Technol., 216 (2015), pp.328-338, https://doi.org/10.1016/j.jmatprotec.2014.09.021.
[45] T.H.C. Childs, Friction modelling in metal cutting, Wear, 260 (2006), pp.310-318. https://doi.org/10.1016/j.wear.2005.01.052.

[46] T.H.C. Childs, A.W. Otieno, Simulations and experiments on machining carbon and low alloy steels at rake face temperatures up to 1200°C, Mach. Sci. Technol., 16 (2012), pp.96-110. https://doi.org/10.1080/10910344.2012.648568.

[47] T.H.C. Childs, P.-J. Arrazola, P. Aristimuno, A. Garay, I. Sacristan, Ti6Al4V metal cutting chip formation experiments and modelling over a wide range of cutting speed J. Mater. Process. Technol., 255 (2018), pp.898-913. https://doi.org/10.1016/j.jmatprotec.2018.01.026.

[48] P.J. Gould, B.D. Goldthorpe, A path-dependent constitutive model for gilding copper, J. Phys. IV France, 10 (2000), pp.39-45. https://doi.org/10.1051/jp4:2000907.

[49] F.J. Zerilli, R.W. Armstrong, Dislocation-mechanics-based constitutive relations for material dynamics calculations, J. Appl. Phys. 61 (1987) pp.1816-1825. https://doi.org/10.1063/1.338024.

[50] M.-H. Nadal, P. Le Poac 46, Continuous model for the shear modulus as a function of pressure and temperature up to the melting point: analysis and ultrasonic validation, J. Appl. Phys., 93 (2003), pp.2472-2480. https://doi.org/10.1063/1.1539913.

[51] A.D. Rollett, U.F. Kocks, A review of the stages of work hardening, Solid State Phenomena, 35-36 (1993), pp.1-18. https://doi.org/10.4028/www.scientific.net/ssp.35-36.1.

[52] L.C. Forde, W.G Proud, S.M. Walley, Symmetrical Taylor impact studies of copper, Proc. Roy. Soc., A465 (2009), pp.769-790. https://doi.org/10.1098/rspa.2008.0205.

[53] P.S. Follansbee, Fundamentals of Strength, John Wiley, Hoboken, NJ, 2014, Ch. 6, Section 5. https://doi.org/10.1002/9781118808412.

[54] L.M. Brown, Unifying concepts in dislocation plasticity, Philos. Mag., 85 (2005), pp.2989-3001. https://doi.org/10.1080/1478643050015460.

[55] Alesa AG, On-line catalogue, accessed 27/11/2019. https://www.alesa.ch/fileadmin/user_upload/kataloge/ALESA_WSP_e.pdf.

[56] T.D. Marusich, M. Ortiz, Modelling and simulation of high speed machining, Int. J. Numer. Methods Eng., 38 (1995), pp.3675-3694. https://doi.org/10.1002/nme.1620382108.

[57] P.-J. Arrazola, P. Aristimuno, D. Soler, T.H.C. Childs, Metal cutting experiments and modeling for improved determination of chip/tool contact temperature by infrared thermography, CIRP Ann. – Manuf. Technol., 64 (2015), pp.57-60. https://doi.org/10.1016/j.cirp.2015.04.061.

[58] M.M. Chaudhri, Subsurface strain distribution around Vickers hardness indentations in annealed polycrystalline copper, Acta mater., 46 (1998), pp. 3047-3056. https://doi.org/10.1016/S1359-6454(98)00010-X.

[59] U.F. Kocks, M.G. Stout, A.D. Rollett, The Influence of texture on strain hardening, In Strength of Metals and Alloys (ICSMA 8), P.O. Kettunen, T.K. Lepisto, M.E. Lehtonen, Eds., Pergamon Press Oxford, 1989, pp. 25-34. https://doi.org/10.1016/B978-0-08-034804-9.50008-5.

[60] T.H.C. Childs, Surface energy, cutting edge radius and material flow stress size effects in continuous chip formation of metals, CIRP J. Manuf. Sci. Technol., 3 (2010), pp. 27-49. https://doi.org/10.1016/j.cirpj.2010.07.008.